**Article:**
Dashti Nafati, M, Kowsari, E, Neekzad, N et al. (5 more authors) (2022) TMP/Pd Complex Immobilized on Graphene Oxide for Efficient Pseudocapacitive Energy Storage with Combined Experimental and DFT Study. Journal of Molecular Liquids, 364. 120008. ISSN 0167-7322

https://doi.org/10.1016/j.molliq.2022.120008

# TMP/Pd Complex Immobilized on Graphene Oxide for Efficient Pseudocapacitive Energy Storage with Combined Experimental and DFT Study

Mohammad Dashti Najafi [a], Elaheh Kowsari [a, 1]*, Nariman Neekzad [a], Seeram Ramakrishna [b, *], Saeedeh Sarabadani Tafreshi [a], Amutha Chinnappan [b], Hamid Reza Naderi [c], Nora H. de Leeuw [d,e]

[a] Department of Chemistry, Amirkabir University of Technology, No. 424, Hafez Avenue, 1591634311, Tehran, Iran

[b] Department of Mechanical Engineering, Center for Nanofibers and Nanotechnology, National University of Singapore, Singapore

[c] Novin Ebtekar Company, Exclusive Agent of Metrohm-Autolab and Dropsens Companies, Tehran, Iran

[d] School of Chemistry, Cardiff University, Main Building, Park Place, Cardiff CF10 3AT, United Kingdom

[e] now at: School of Chemistry, University of Leeds, Leeds LS2 9JT, United Kingdom

[1] * Corresponding authors

*E-mail addresses:* Kowsarie@aut.ac.ir (E. Kowsari) and seeram@nus.edu.sg (S. Ramakrishna)

**Abstract**

Designing sophisticated energy sources that can offer a large amount of electricity for various energy storage uses is a pressing need. In this study, Trimethoprim (TMP) was functionalized as a rich supply of nitrogen and oxygen on graphene oxide (FGO-TMP), using graphene oxide layers adorned with trimethoprim functional groups. Then, using a simple approach to synthesize FGO-TMP/Pd complex for supercapacitor applications, palladium ions were reacted and fixed on the FGO-TMP composite surface. The FGO-TMP/Pd composite produced was characterized as a symmetric capacitor with a capacitance of 330 F $g^{-1}$ at 5 mV $s^{-1}$ and high energy and power densities of 60.3 W h $Kg^{-1}$ and 1200 W $kg^{-1}$, respectively. After 10000 cycles at 8 A $g^{-1}$, this symmetric device retained 93.7 percent of its original capacitance, proving the remarkable capacitive performance of the developed platform as well as ultra-stability for such sophisticated energy storage devices. Topological analysis of the electron density distribution and its Laplacian at the bonding critical points and Bader atomic charges of the GO layer in both FGO-TMP and FGO-TMP/Pd composites confirms more concentrated bond charges in FGO-TMP/Pd, indicating effective improvement in electrode material behavior in a supercapacitor.

**Keywords:** functional groups, palladium ions, symmetric capacitor, energy applications, topological analysis

## 1. Introduction

High energy demand, limited natural fossil fuel supplies, and environmental concerns have prompted extensive research and development efforts to advance effective electrode components for new energy storage and conversion systems with maximum electrochemical capability, including environmentally sustainable materials and low-cost synthesis methods[1–3]. Because of their effective charging/discharging mechanism, high power capacity efficiency, low maintenance

requirement, and long lifespan, supercapacitors (SCs) have emerged as high electrochemical potential systems frequently used in the setup of high-power applications and kinetic energy transfer. The stored energy in SCs is often caused by ion adsorption at the electrolyte/electrode interfaces and a rapid faradic redox process in the bulk electrodes[4–6]. The design and manufacture of efficient electrode materials have sparked a lot of attention in terms of having quick energy storage at a high charge-discharge current density to improve the pseudocapacitive behavior of SCs devices[7]. Carbon fibers, carbon aerogels, activated carbon, carbon nanotubes, and porous graphene are among the carbon-based materials that have been reported to have a large surface area and excellent electrical conductivity[8–17]. Conducting polymers (CPs) and transition metal oxides (TMOs) have also been widely used as supercapacitor electrode materials[18–20]. Graphene has gained interest in the domain of SCs electrode material investigation because of its 2D nanostructure, high theoretical gravimetric capacitance, theoretical surface area (2600 $m^2$ $g^{-1}$), thermal conductivity, and mechanical stability [21,22]. Its unique property might significantly improve the electrochemical efficiency of SCs, making it a suitable electrode material for SC applications[23]. Graphene oxide (GO), reduced graphene oxide (rGO), and functionalized reduced graphene oxide (F-rGO) have all been used as independent electrodes in EDLC SCs[24,25]. To improve the electrochemical behavior of capacitive performance, the loading of metal and metal oxide with graphene and its derivatives might prevent them from restacking, making them excellent candidates for high-performance SCs[26]. Meanwhile, numerous noble metals, including ruthenium (Ru)[27,28], nickel (Ni)[29,30], platinum (Pt)[31,32], and gold (Au)[33,34], have succeeded to develop in energy storage systems with graphene derivatives. Despite the fact that there have been few studies on graphene/Pd electrode materials in SCs, the current research might become a significant topic in the next years. Kalambate et al. recently

employed a two-step approach to creating a composite of N-GNS-PdNP-PANI that delivered 230 F $g^{-1}$ capacitance and kept 96 percent of its total capacitance following 3000 prolonged cycles[35]. Wei et al. used a PdPGO composite electrode material inside a symmetric device to achieve a capacitance of 595 F $g^{-1}$ at 1 A $g^{-1}$. Capacitance retention measured as 88 percent after 5000 cycles[36]. In another work, Kumar et al. used an electrochemical synthesis method to create hybrid electrodes of rGO nanosheets and palladium nanoparticles as effective materials in symmetric supercapacitors. The assembled three-electrode device demonstrated a phenomenal capacitance of 1524.7 F $g^{-1}$ at a scan rate of 20 mV $s^{-1}$ and enhanced cycle life (92.1 percent; 2000 cycles). This research created a new technique for making Pd-E-ErGO composites using in-situ electrochemical reduction and electrode material deposition, which might be useful in next-generation enhanced electrochemical capacitors[37]. Kim et al. employed an efficient microwave approach to fabricate electrodes of 3D G-CNT-Pd nanostructures with an excellent specific capacity of 1615 F $g^{-1}$ at 10 mV $s^{-1}$, an extremely high oxidation/reduction capacitance owing to high porosity, a high ratio of specific surface area, and capacitance-like redox responding of the palladium nanoparticles [38]. In the present research, we designed and developed a simple method for synthesizing FGO-TMP in which TMP functional groups were covalently functionalized GO and then $Pd^{2+}$ ions were reacted and adsorbed on the surface of the FGO-TMP composite. A DFT investigation, different surface analysis methodologies, and electrochemical studies were used to evaluate the synthesized FGO-TMP and FGO-TMP/Pd composites. The electrode material is made using an efficient, flexible, and low-cost electrodeposition method on a piece of stainless steel that acts as the current collector. Furthermore, the porous structure of GO sheets is prevented from aggregating by the TMP and TMP/Pd composite, allowing the electrolyte to permeate into the electrodeposited composite. Meanwhile, a symmetric SC was built and evaluated in 1M $H_2SO_4$

electrolyte utilizing FGO-TMP/Pd electrode. With a large capacitance value of 687 F $g^{-1}$ and remarkable cycle life (95.8 percent; 10000 cycles) over a long time, while retaining good rate capability, the FGO-TMP/Pd composite represents a significant improvement in the electrochemical performance of SCs. This also means that the FGO-TMP and FGO-TMP/Pd composites have good electrochemical connections, high specific capacitance and cycle endurance.

## 2. Experimental

### *2.1. Materials*

All compounds utilized in this study were selected from high-quality analytical-grade substances and purchased from Sigma-Aldrich. In the following tests, double-distilled water was also used.

### *2.2. Synthesis of GO*

The production of GO powder from natural graphite was done using a modified Hummers method. In order to regulate the temperature, 2 g graphite powder, and 1.5 g $NaNO_3$ were blended in a 1L container, then 67.5 ml concentrated $H_2SO_4$ was added and agitated in an ice bath. The mentioned mixture was then gently added 9 g of $KMnO_4$ and stirred for 2 hours before being kept at 20 °C for 5 days with continual stirring to generate a viscous brownish liquid. After that, the mixture was agitated for 1 hour while 200 ml of $H_2SO_4$ (5 wt percent) aqueous solution was added dropwise. The resultant precipitate was washed numerous times with 6ml $H_2O_2$ (30 percent aqueous solution) and double distilled water to remove manganese, permanganate the remaining ions, and purify it further. GO was eventually vacuum dried[39–41].

### *2.3. Synthesis procedure of FGO-TMP and FGO-TMP/Pd*

FGO-TMP was synthesized by acylating GO with thionyl chloride ($SOCl_2$) in a two-step esterification method. Firstly, powdered graphene (1.5 g) was dissolved in 60 mL $SOCl_2$ at 70 °C, resulting in a suspension that was refluxed for 1 day in a nitrogen environment. The excess quantity of $SOCl_2$ was efficiently eliminated by adding tetrahydrofuran to the mixture described above and allowing it to run through a filter column. The generated GO-Cl (3 g) was then dissolved in a solution of trimethoprim (2.9 g) and dimethyl sulfoxide (DMSO) (60 mL) and kept at 80 °C for 2 days in a neck flask connected to a refluxing device under a nitrogen atmosphere. After that, the remnant solid-state substance was cooled to room temperature after being filtered and washed with water and methanol many times to eliminate any remaining agent. TMP covalently functionalized GO was obtained after progressively vacuum drying the nanoplatelets (FGO-TMP). The FGO-TMP/Pd combination was made by reacting $Pd(NO_3)_2$ (5 mmol) with FGO-TMP (4.02 g) in methanol in a simple one-step procedure (50 ml). After that, the reaction mixture was cooled and kept at 25°C for 2 days after being refluxed at 65°C for 4 hours. The black precipitate was filtered before vacuum dried after being washed twice with ethanol (Fig. 1).

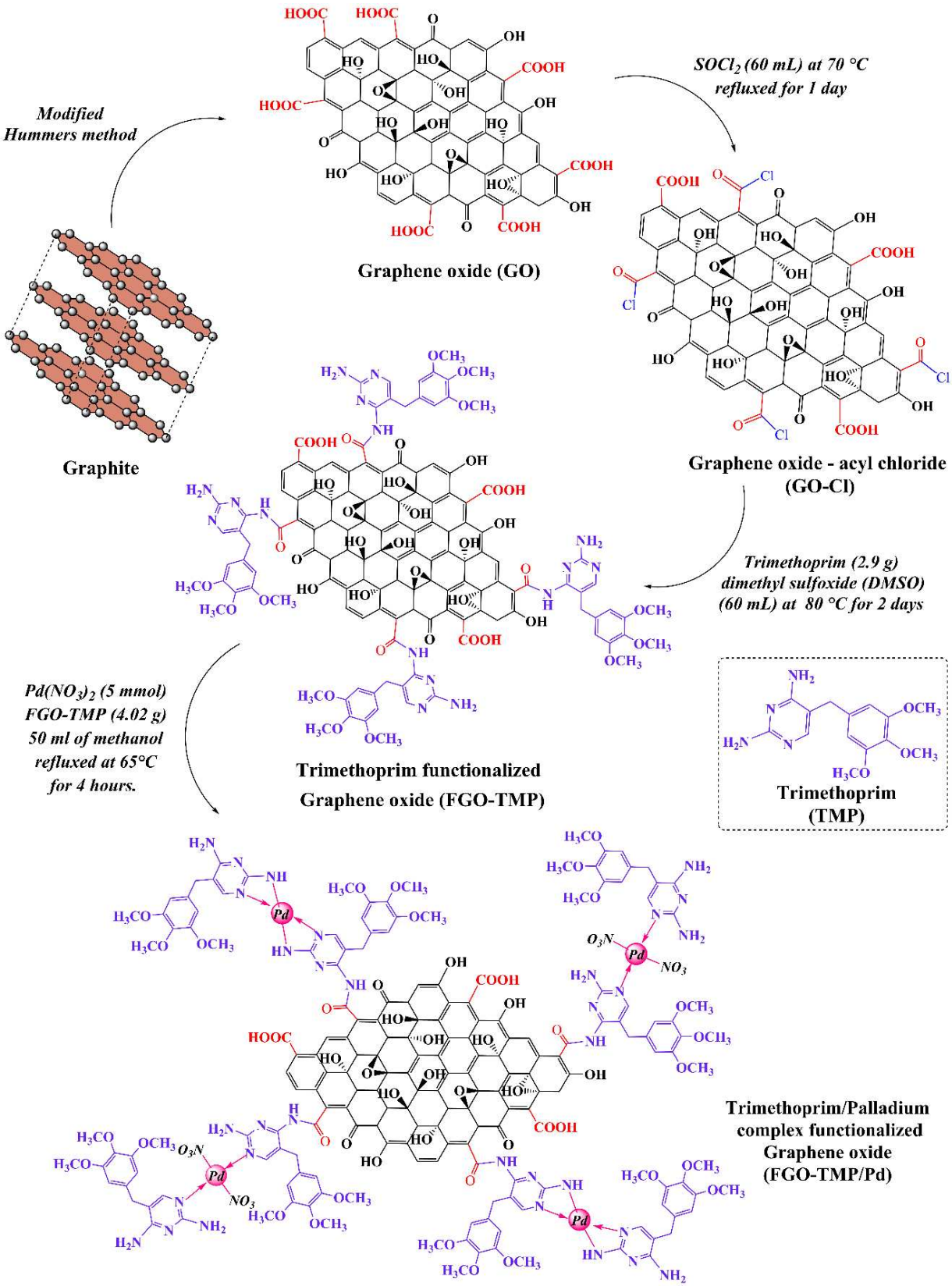


**Fig. 1.** All FGO-TMP and FGO-TMP/Pd synthesis procedures are shown in this schematic.

## 3. Instrumentation

### *3.1. Characterization*

The efficacy of produced materials was assessed using a variety of characterization approaches. FT-IR (Thermo Nicolet Avatar 360), XRD (INEL, Equinox 3000), and Raman spectroscopy (Almega Thermo Nicolet) were used to evaluate the materials generated in this case. The gadget was chosen as Quantera II (Physical Electronics, Minneapolis, Minnesota, USA). On samples, XPS (Bes-Tec photoelectron spectrometer) examination was done with monochromatic Al KR (1486.6 eV) irradiation. The surface area of synthetic materials was investigated using the BET (BELSORP-mini II) technology. FE-SEM (Mira III LM, Tuscan) and TEM (model Zeiss-EM10C Company) were used for morphological assessment of materials. Standard assessment procedures were used for all of the studies.

### *3.2. Electrochemical setup*

Electrochemical methods in general (CV, GCD, and EIS) were carried out in 1M $H_2SO_4$ electrolyte using an electrochemical workstation (Ivium V21508, Vertex). A combination of samples (FGO-TMP and FGO-TMP/Pd) were combined and dispersed in ethanol with carbon black (20%), graphite (15%), and polytetrafluoroethylene (PTFE) to make the working electrodes (5 percent). A uniform mixture (1 mg) was then squeezed onto a rustproof steel piece with a 1 $cm^2$ current collector. The constructed working electrode served as both the positive and negative electrodes in the two-electrode symmetric system. Also, a polypropylene (PP) film was used as the separator and immersed in a 1M $H_2SO_4$ solution. It is important to remember that the mass of SSC devices was similar to that of three-electrode cells[42]. CV measurements may be used to calculate the specific capacitance (Cs) of sample electrodes using the following equation 1[43,44]:

$$C_s = \frac{\int I \, dV}{m \, v \, \Delta V} \qquad (1)$$

where I denotes the current (A), v denotes the potential (V), V denotes the potential window (V), v denotes the scan rate (mV $s^{-1}$), and m denotes the mass (g) of electroactive materials put on the electrode. Equation 2[45,46] was used to compute the specific capacitance (C) values of electrodes using GCD data in order to verify the results.

$$C = \frac{I\,\Delta t}{\Delta V\, m} \qquad (2)$$

Where I signifies discharge current (A), t denotes interval time (s), ΔV denotes potential discharge duration decrease (V), and m denotes active material mass (g) on the electrode surface. Equation 3[47] may also be used to obtain the capacitance values for a single electrode:

$$C_{electrode} = \frac{4\,C_{device}}{m} \qquad (3)$$

where $C_{device}$ signifies the anticipated capacitance of a two-electrode configuration and m denotes the mass of active materials in both electrodes. Equations 4 and 5 were used to obtain the energy and power density values for further electrochemical investigations, respectively[47,48].

$$E_d(W\ h\ Kg^{-1}) = \frac{1}{7.2}\,C_{device}\,.\Delta V^2 \qquad (4)$$

$$P_d(W\ Kg^{-1}) = \frac{E_d \times 3600}{\Delta t} \qquad (5)$$

Where $E_d$, $\Delta t$, $C_{device}$, $P_d$, $\Delta V$ and are energy density, discharge duration, total specific capacitance value, power density, and potential variation, respectively.

Based on linear Randles-Sevcik equation 6, the slope of peak current vs. square root of the scan rate is equal to the real surface area of the electroactive material deposited on the surface of the electrode[49]:

$$I_p = (2.69 \times 10^5).\ n^{3/2}.\ A.C.\ D^{1/2}.\ v^{1/2} \qquad (6)$$

Where n represents the total number of contributed electrons in a redox reaction, which is commonly set equal to 1, A is the area of the electrode ($cm^2$), C is the electroactive species concentration in solution ($mol/cm^3$), D is the diffusion coefficient ($cm^2/s$), and $v$ is the scan rate (V/s).

*3.3. Computational Details*

The theoretical charge density distribution of the FGO composites was calculated using Bader's Atoms in Molecules (AIM)[50] analysis, density functional theory (DFT)[51,52], and the B3LYP [53] hybrid functional in the Vienna Ab Initio Simulation Package VASP[54,55] with dispersion correction[56]. The topological characteristics and electron density distribution of FGO-TMP and FGO-TMP/Pd composites at the bond critical points (bcp) of the GO layer of both complexes are calculated using the AIM-UC[57] package using the charge density information acquired via VASP optimization. We also used Bader tools from the Henckelman group to compute atomic charges.

## 4. Results and Discussion

XPS analysis is used to explore the chemical nature and binding energies of the bonds present on the surface of GO, FGO-TMP, and FGO-TMP/Pd and the surface chemical state and chemical composition of the materials (Fig. 2a). The CasaXPS software (version 2.3, 2018) that comes with the XPS method is used to evaluate the spectra. Fig. 2a indicates the presence of O1s (26.47 percent) and C1s (73.53 percent) in the GO findings. C1s (80.88, 79.81 percent), O1s (17.08, 16.77 percent), and N1s (2.03, 2.99 percent) are the percentages of components in FGO-TMP and FGO-TMP/Pd. As a result, the proportion of Pd 3d in FGO-TMP/Pd is 0.44 percent, indicating that the

Pd complex is present. The presence of primary components of produced samples evaluated as C 1s (284.3 – 284.2 eV), O 1s (532.3 – 532.2 eV), N 1s (399.3 – 399.2 eV), and Pd 3d seems to be worth noticing (339.2 eV). The C 1s peaks of FGO-TMP and FGO-TMP/Pd composite were compared by deconvoluting each spectrum, as shown in Fig. 2b and 2c, respectively. The deconvolution of the C1s peak of FGO-TMP shows the peaks at 284.6, 284.9, 285.9, 286.8, 288.08, and 289.07 eV corresponding to the C-C, C-OH, C-N, C=O, C(O)N, and C(O)O. Fig. 2c shows the peak of C 1s for the FGO-TMP/Pd, which itself includes six peaks at C-C (284.5), C-OH (284.8), C-N (285.8), C=O (286.6), C(O)N (288.1), and C(O)O (289.1) eV. The N 1s region spectrum is deconvoluted for FGO-TMP and FGO-TMP/Pd in three and four type peaks of nitrogen, respectively. As shown in Fig. S1a, the peaks at 400.4, 398.6, and 405.1 eV are due to the presence of N-C, N=C, and N-H bonding. The N1s deconvolution peaks for the FGO-TMP/Pd include N=C (400.8), N-C (400.2), and N-H (406.6) eV (Fig. S1b)[58]. The N-Pd group may be responsible for appearing a new distinct peak in the N1s spectrum at 401.8 eV, demonstrating that nitrogen was effectively doped with palladium in FGO-TMP/Pd. As may be seen in Figures S1c and S1d, The binding energies of C=O (531.3, 531.3), C-OH (532.3, 532.1), and C-O-C (533.1, 533.3) were also shown by the O1s deconvolution peak for the FGO-TMP and FGO-TMP/Pd. Pd $3d_{5/2}$, Pd $3d_{3/2}$, and Pd-N were assigned to the binding energies of Pd 3d for FGO-TMP/Pd shown by the untreated substrate at 337.7, 342.6, and 339.2 eV, respectively (Fig. 2d)[59].

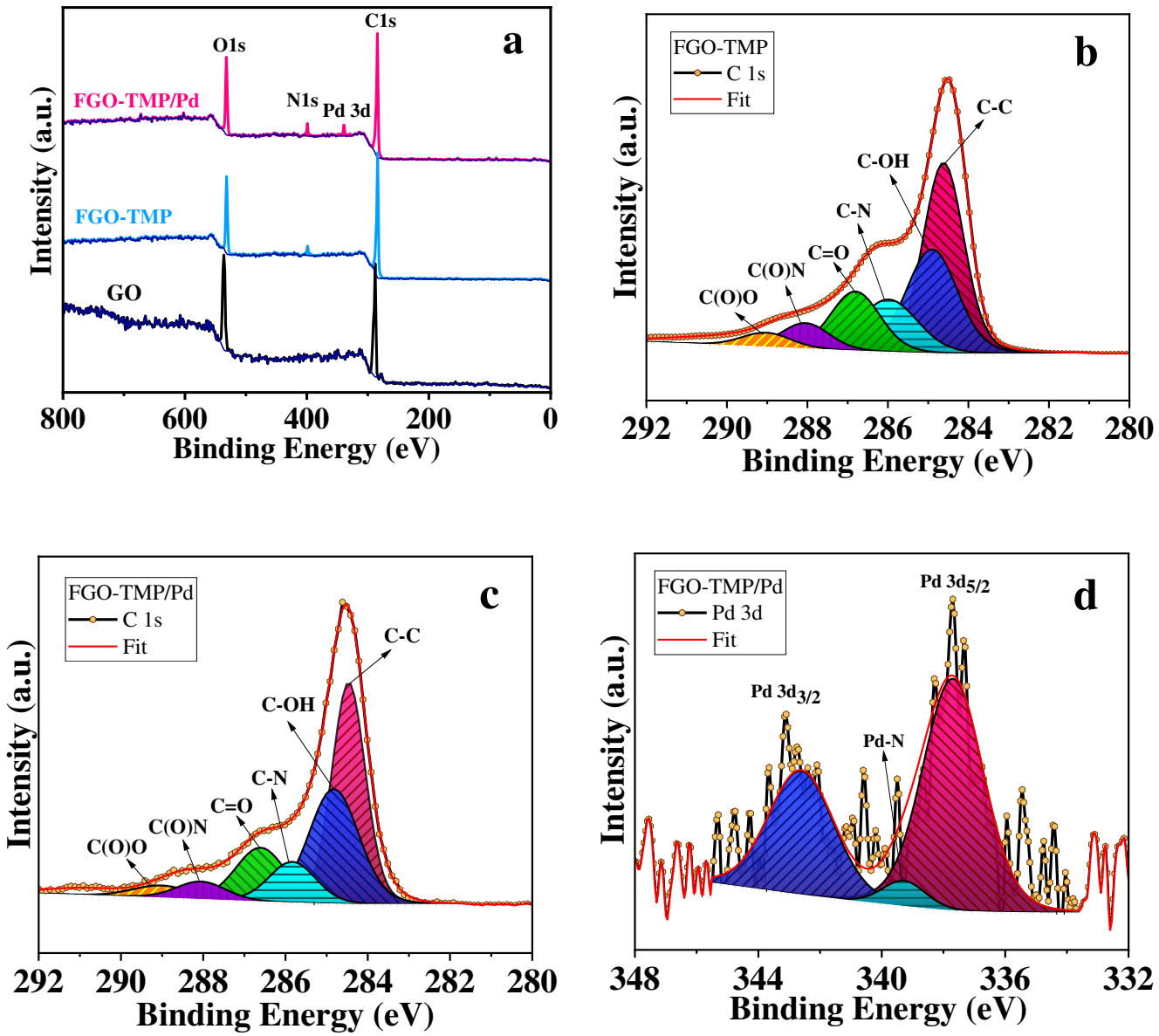


**Fig. 2.** (a) Full range XPS spectra of GO, FGO-TMP, and FGO-TMP/Pd; (b) Deconvolution of C 1s spectra of FGO-TMP; (c) Deconvolution of C 1s spectra of FGO-TMP/Pd; and (d) XPS of Pd 3d (FGO-TMP/Pd).

The specific surface area and pore size distribution of the GO, FGO-TMP, and FGO-TMP/Pd composite are further examined using $N_2$ adsorption-desorption analysis to better understand the

charge storage mechanism. According to IUPAC regulations, all synthesized materials showed a similar adsorption isotherm, which could be categorized as type III (Fig. 3a). Mesoporous and microporous synthesized materials frequently give this classification[39]. Table S1. shows the structural differences between the three samples. The surface areas of FGO-TMP and FGO-TMP/Pd BET were found to be 49.776 and 71.351 $m^2/g$, respectively, while the surface area of GO was only 24.188 $m^2/g$.

Furthermore, the micropore size distributions of the three samples are similar, with the most micropores measured between 1.2 and 1.8 nm[60]. The pattern of pore size observed further supports these conclusions (presented in Fig 3a). Because of the functionalization of GO with TMP and TMP/Pd ligands, the pore volume of FGO-TMP and FGO-TMP/Pd has increased compared to GO (Fig. 3a).

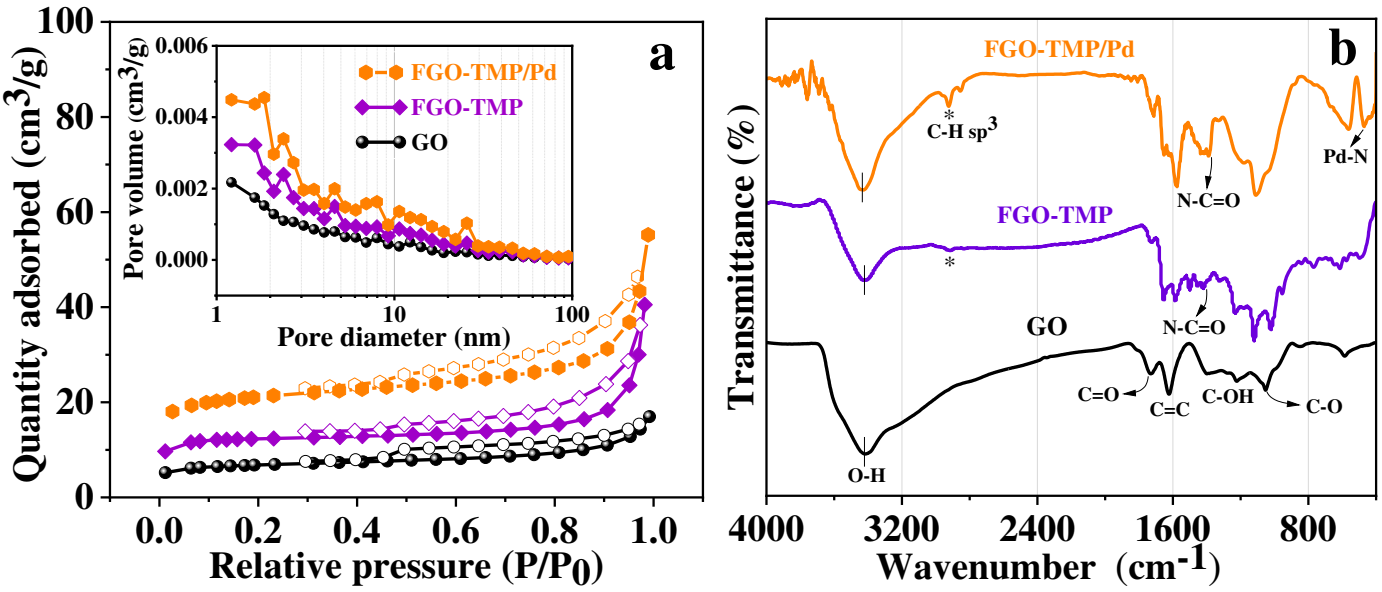

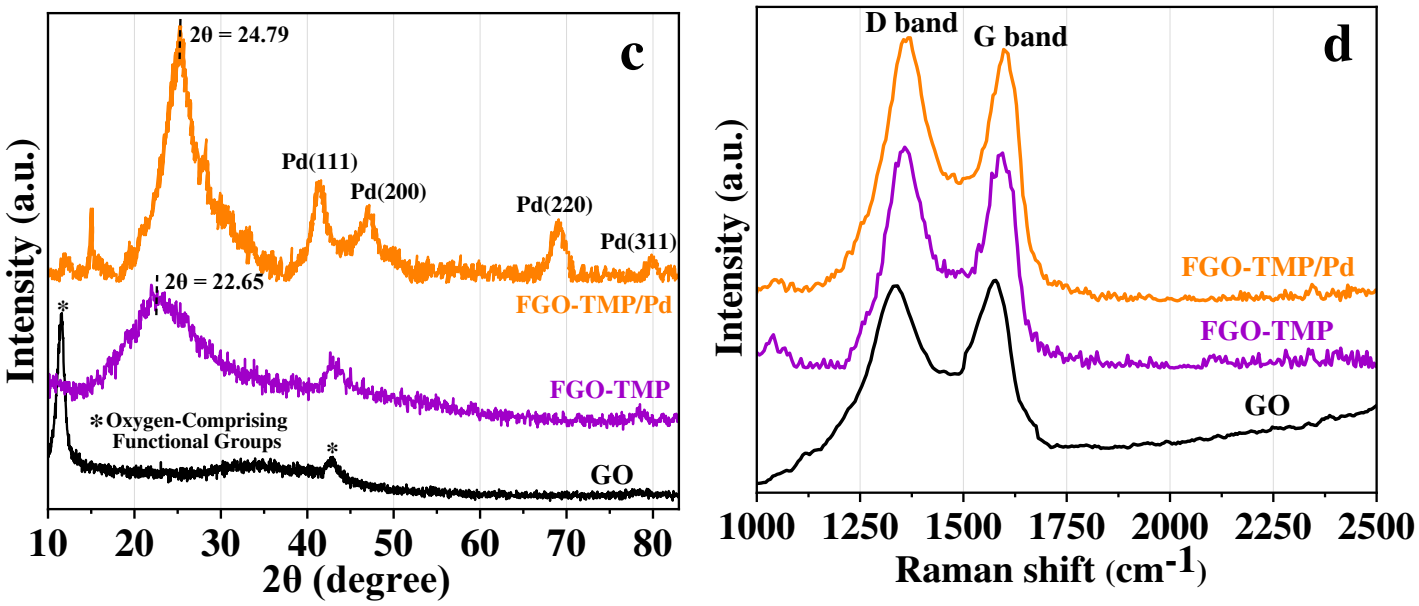


**Fig. 3.** (a) $N_2$ adsorption/desorption isotherms and pore size distribution (BJH) for GO, FGO-TMP, and FGO-TMP/Pd composite; (b) FT-IR of GO, FGO-TMP, and FGO-TMP/Pd composite; (c) XRD diffractogram of GO, FGO-TMP, and FGO-TMP/Pd composite; (d) Confocal Raman spectroscopy results of GO, FGO-TMP, and FGO-TMP/Pd composite.

For pure GO, FGO-TMP, and FGO-TMP/Pd, FTIR spectra in the 4000-400 $cm^{-1}$ region are shown in Fig. 3b. Oxygen-derived groups are visible in the GO spectrum. For the FTIR spectrum of GO, the stretching of C=O, C-O-C, C-O, and C-OH bonds related to the epoxide was located at 1724, 1219, 1048, and 1377 $cm^{-1}$, respectively. In this case, each appeared peak arises from the C-C stretching vibration (1471 $cm^{-1}$) and stretching vibration of the C=C group of GO (1570 $cm^{-1}$). The peaks at 1570 and 1471 $cm^{-1}$ indicate the C=C and C-C bonds in the GO[61]. According to the FGO-TMP and FGO-TMP/Pd spectrum, the new peaks can be seen at 2914-2923 $cm^{-1}$ and 1330-1332 $cm^{-1}$, which correspond to the stretching of C-H $sp^3$ and C–N. The bonds identified at 1410 and 1390 $cm^{-1}$ (N-C=O stretching) show that TMP and TMP/Pd were successfully attached to GO.

Fig. 3b shows the Pd-N vibration peak at 472 $cm^{-1}$ with other typical GO bonds, supporting the FGO-TMP/Pd complex's lucrative functionalization route[62,63].

The XRD patterns of the GO, FGO-TMP, and FGO-TMP/Pd are given in Fig. 3c. The GO showed a prominent diffraction peak at 2ɵ =11° and 43°, respectively, when interlayer distances were 0.79 and 0.21 nm. An increased basal distance is caused by the effective insertion of distinct groups of hydroxyl, carbonyl, and epoxide on the outer side of GO. The total diffraction intensity of graphene oxide was reduced due to the chemical functionalization. Two maximums with identical widths have been observed for FGO-TMP and FGO-TMP/Pd at 22.65° and 24.79°, respectively, equating to d-spacing of 3.9 and 3.6 nm. In the FGO-TMP/Pd spectrum (JCPDS no. 01-087-0645)[37], diffraction peaks at 40.98°, 46.84°, 69.19°, and 79.84° are connected to the (111), (200), (220), and (311) crystallographic planes of the facing centered cubic structure of the Pd nanoparticles, respectively. The computed peaks at 2ɵ of 8.38°, 38.48°, and 78.42° for FGO-TMP and 2ɵ of 12.03°, 15.18°, 28.38°, and 30.18° for FGO-TMP/Pd indicate the production of monoclinic crystals of TMP and TMP/Pd. These peaks imply that functional groups at the GO surface have successfully covalently bonded[64].

To further understand the interaction between the TMP and TMP/Pd in the FGO-TMP and FGO-TMP/Pd composites, Raman spectroscopy was used, and the corresponding Raman spectra of the FGO-TMP and FGO-TMP/Pd composite with that of GO are shown in Fig. 3d. GO shows peaks at 1341 and 1573 $cm^{-1}$ corresponding to the D-band and G-band, respectively. The Raman peaks at 1358, and 1366 $cm^{-1}$ in Fig. 3d correspond to the D-band of FGO-TMP and FGO-TMP/Pd, respectively, for the mode of breathing generated by $sp^2$ ring defects[34]. The FGO-TMP and FGO-TMP/Pd show similar peaks corresponding to the G-band but with an ID/IG ratio increase from 0.985 for GO to 1.027 and 1.046 for FGO-TMP and FGO-TMP/P, respectively. The D peak

in graphite whiskers is tied to the peaks reported in FGO-TMP and FGO-TMP/Pd at 1040 and 1059 $cm^{-1}$[65].

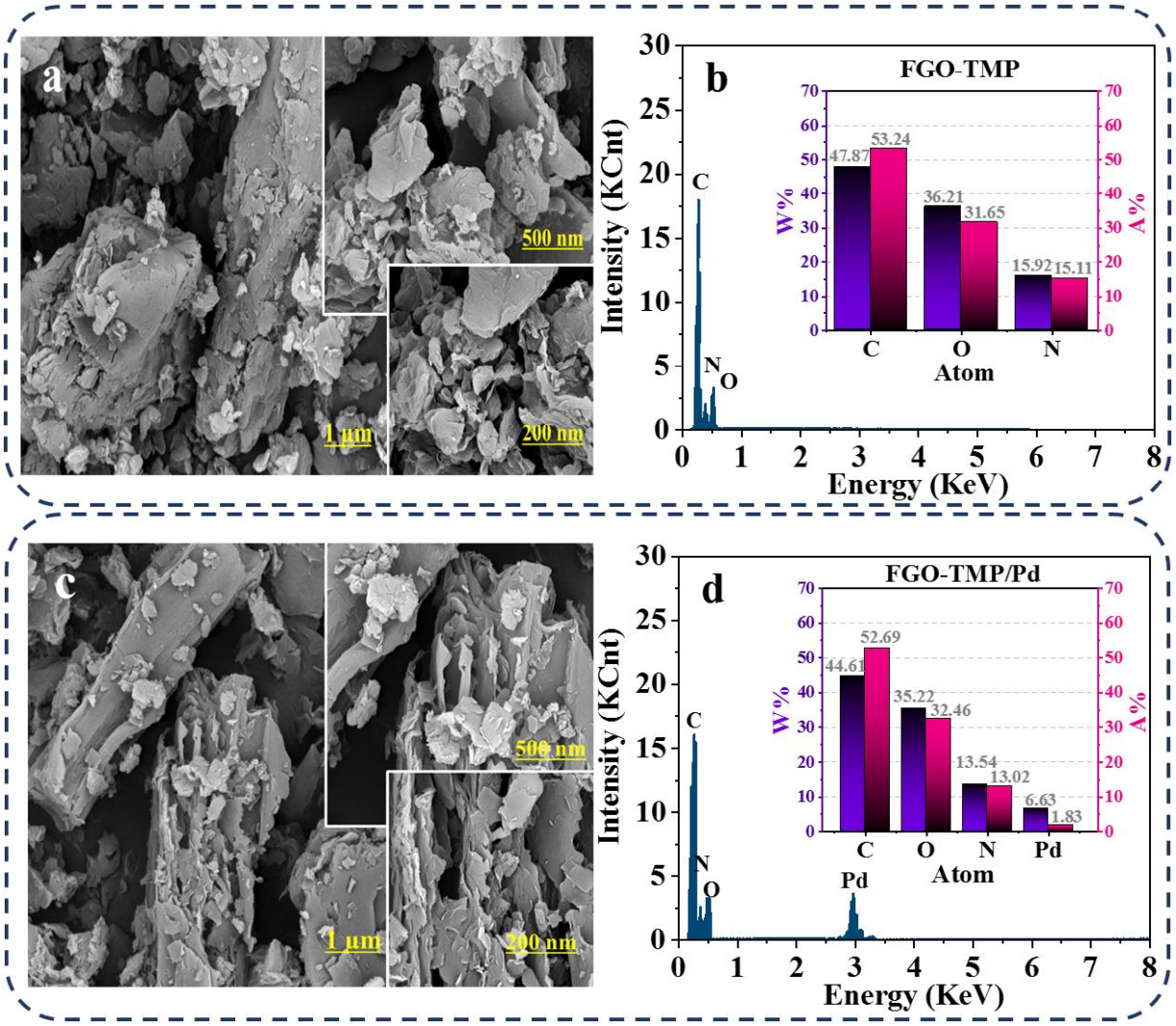


**Fig. 4.** FE-SEM images of a) FGO-TMP and c) FGO-TMP/Pd composite; EDX analysis with inset showing the mass and atomic percentage of b) FGO-TMP and d) FGO-TMP/Pd composite.

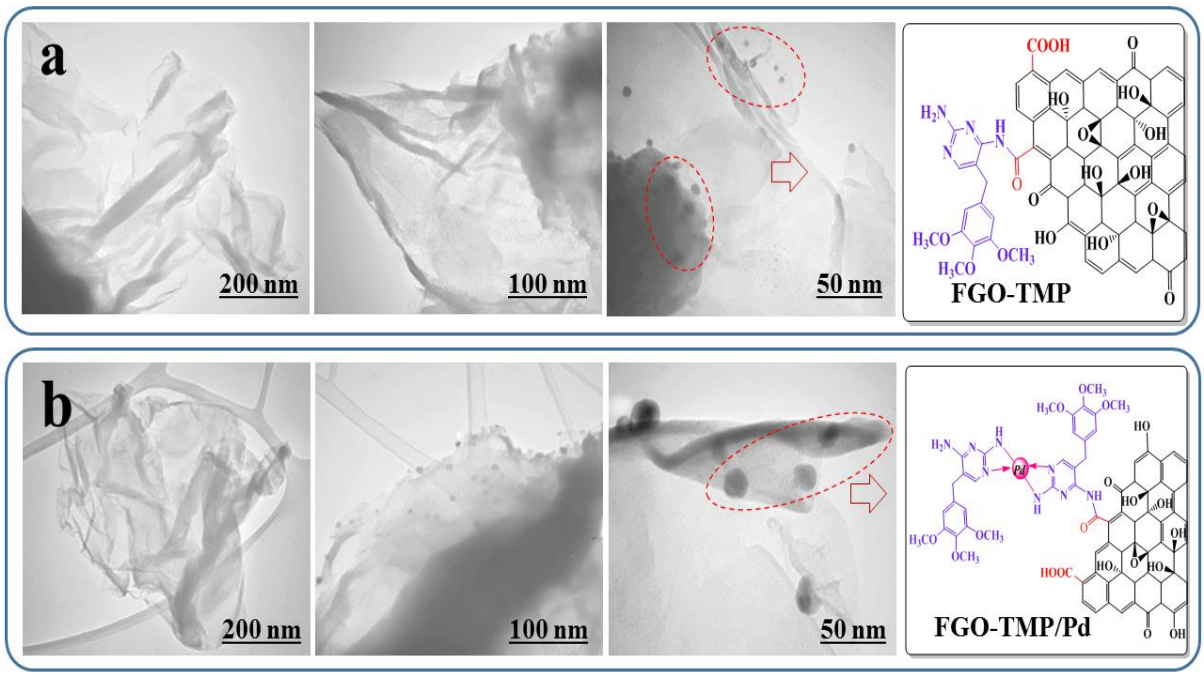


**Fig. 5.** TEM Images of a) FGO-TMP and b) FGO-TMP/Pd composite.

FE-SEM is a valuable tool for determining material morphology since it takes into account the effects of functionalization and accelerating variables on particular structures. Fig. 4a and 4c show the overall morphology of the as-synthesized FGO-TMP and FGO-TMP/Pd composites. The typical thickness of pores is between 10 and 500 nanometers. The presence of C, N, Pd, and O is further confirmed by EDX investigation of FGO-TMP and FGO-TMP/Pd shown in Fig. 4b and 4c. The images of EDX mapping of the FGO-TMP/Pd composite are indicated in Fig. S2. According to the pictures, C, N, O, and Pd atoms have similar element distribution, showing the uniform dispersion of Pd atoms. TEM photos of the intensity of the electron attenuated by FGO-TMP and FGO-TMP/Pd platelets with varying thickness diameters are shown in Figs. 5a and 5b. This implies a sheet-like shape with varied transparencies of roughly 200, 100, and 50 nm in the investigated region. The dark patches depict a dense nanostructure of multiple GO or GO layers with diverse oxygen functional groups stacked together[66].

## 5. Computational Results

By adding TMP functional groups to the GO layer, we developed FGO-TMP and FGO-TMP/Pd composites. We added four TMP groups to the GO sheet in each compound in order to consider various TMP/Pd complexes on the GO layer of FGO-TMP/Pd and have the same amount of TMP on both FGO-TMP and FGO-TMP/Pd. The minimum energy structures of FGO-TMP and FGO-TMP/Pd used in our calculations are shown in Fig. S3a and S4a, respectively, where their components include the GO layer, TMP, and TMP/Pd groups. For clarity, the minimum energy structures of FGO-TMP and FGO-TMP/Pd used in our calculations are shown in Fig. S3b and S4b. Analysis of the topology of electron density bcp(r) and its Laplacian 2bc(r) at bonding crucial points (bcp) of FGO-TMP and FGO-TMP/Pd composites was carried out based on Bader's AIM to shed additional insight on the charge density distribution and atomic charges of the FGO-TMP/Pd electrode in SC devices. The values and discrepancies of bcp(r) and 2bc(r) of C-C and C-H bonds of the GO layer of FGO-TMP and FGO-TMP/Pd composites are shown in Table S2 and Fig. 6, respectively. The ranges of electron density and Laplacian of C-C and C-H bonds of GO layer of FGO-TMP-Pd complex are 1.631 to 2.325 $eÅ^{-3}$ and -13.397 to -30.397 $eÅ^{-5}$ with an average of 1.999 $eÅ^{-3}$ and -24.683 $eÅ^{-5}$ compared to ranges of 1.691 to 2.308 $eÅ^{-3}$ and -15.407 to -29.989 $eÅ^{-5}$ and average of 1.996 $eÅ^{-3}$ and -24.594 $eÅ^{-5}$ on FGO-TMP, respectively.

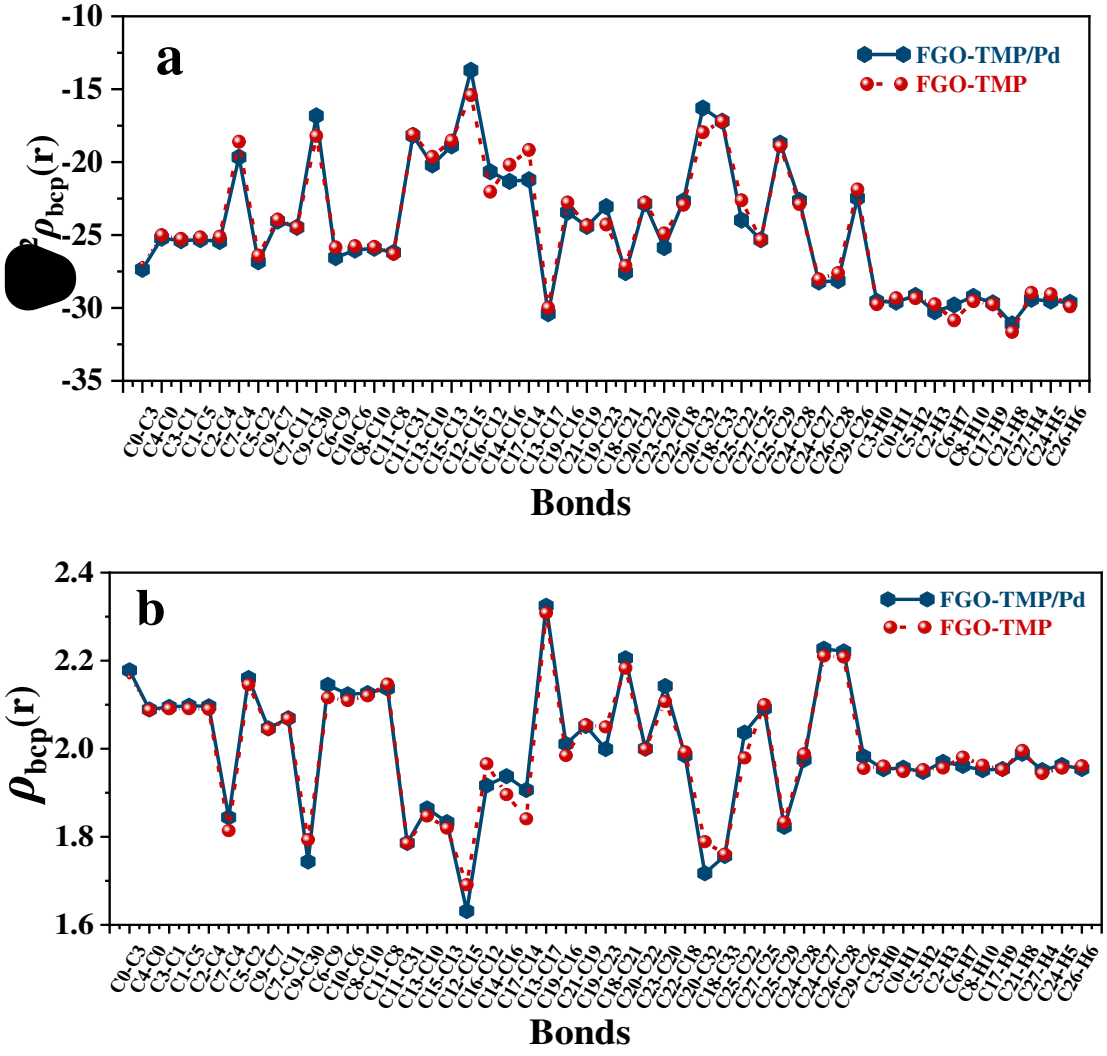


**Fig. 6.** The differences of (a) the Laplacian of electron density $\nabla^2\rho_{bcp}(r)$ and (b) electron density $\rho_{bcp}(r)$ of carbon atoms of GO layer of FGO-TMP and FGO-TMP/Pd complexes. To find the atoms refer to Fig. S5.

In Fig. 7, we also displayed $\nabla^2\rho_{bcp}(r)$ of the GO layer of FGO-TMP/Pd, which shows strong charge density accumulation between the bonds, with positive and negative contours indicating charge concentration and depletion, respectively. Table S3 shows the findings of Bader charge and atomic volume analyses of carbon, oxygen, and hydrogen atoms in the GO layer of both FGO-TMP/Pd and FGO-TMP complexes. On the GO layer of the FGO-TMP/Pd and FGO-TMP structures, the average charge of the atoms is -0.293 and -0.276e, respectively, demonstrating that the FGO-

TMP/Pd composite has greater charges. The more electronegative oxygen atoms have higher volume as well as more negative charges, according to the examination of each atom volume. The increased average electron density, Laplacian, and atomic charges values of the GO layer in the FGO-TMP/Pd composite illustrate that the bonding charges in this compound are more localized than those in FGO-TMP, suggesting a significant improvement in the behavior of the electrode material in a supercapacitor.

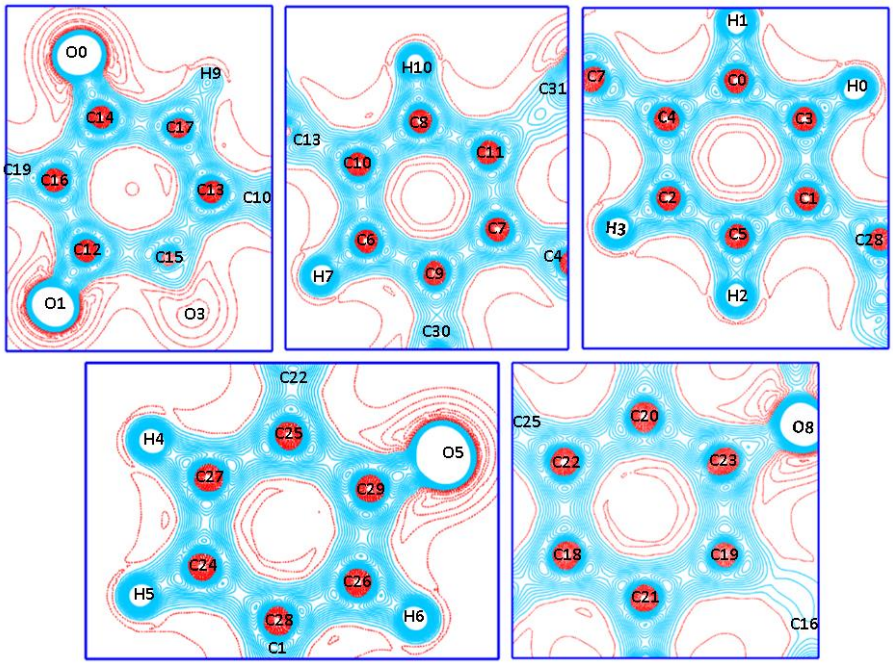


**Fig. 7.** In the light of the AIM theory, the contour line plot of Laplacian of electron density of five phenyl rings of the GO layer of FGO-TMP/Pd produced from theoretical charge density. Contours are drawn in 3 $eÅ^{-5}$ intervals. Positive Laplacian values are shown by solid blue lines, whereas red dotted lines represent negative Laplacian values. Refer to Fig. S5 to locate the atoms.

## 6. Electrochemical Measurement

The capacitance efficiency of the FGO-TMP and FGO-TMP/Pd complex was studied using cyclic voltammetry (CV), galvanostatic charge-discharge (GCD), and electrochemical impedance spectroscopy (EIS) in a three-electrode setup with 1 M $H_2SO_4$ solution. Figures 8a and 8b show CV evaluations and measurements of produced electrode samples recorded at scanning speeds of 5-100 mV $s^{-1}$. The measured profiles of CV maintain their quasi-rectangular shape as the scanning rate increases (5 to 100 mV $s^{-1}$), confirming their high-rate performance and capacitive qualities. A more rectangular shape was also shown to result in lower charge transfer resistance and, as a result, a faster rate of ion diffusion[30]. In the voltage range, -0.5 V to 0.7 V, the CV curve of FGO-TMP/Pd has a larger rectangular area, clearly suggesting that the composite has superior EDLC behavioral patterns. Meanwhile, in the potential range of -0.3 V to 0.6 V, the FGO-TMP CV curve seems to have weak redox peaks, indicating pseudocapacitance behavior. FGO-TMP/Pd utilizes both the pseudocapacitor and the EDLC processes for energy storage, while FGO-TMP exclusively uses the EDLC mechanism. The CV curves for FGO-TMP and FGO-TMP/Pd complex are shown in Fig. 8c at the same scan rate (5 mV $s^{-1}$) for comparison. For FGO-TMP and FGO-TMP/Pd electrodes, the highest computed specific capacitance values were 315 and 687 F $g^{-1}$, respectively, at 5 mV $s^{-1}$. FGO-TMP and FGO-TMP/Pd complex capacitance decreased as the number of scan rates increased (Fig. 8d).

The Randles-Sevcik plots of FGO-TMP and FGO-TMP/Pd complex are exhibited in Fig. 8e. As the scan rate is grown from 5 to 100 mV $s^{-1}$, the peak current ($I_p$) enhances. More notably, $I_p$ differs linearly with the square root of the scan rate ($v^{1/2}$), as reported by the Randles-Sevcik equation (6). These observations suggest that redox reactions at the electrode-electrolyte interface are fast and quasi-reversible and are only limited by electrolyte diffusion. As a result, as indicated in Fig. 8e, it is evident that the slope achieved for FGO-TMP/Pd is about 4 times higher than FGO-TMP. This

may be seen as an essential indication of the increase in the specific surface area value when TMP/Pd is introduced to GO. [67].

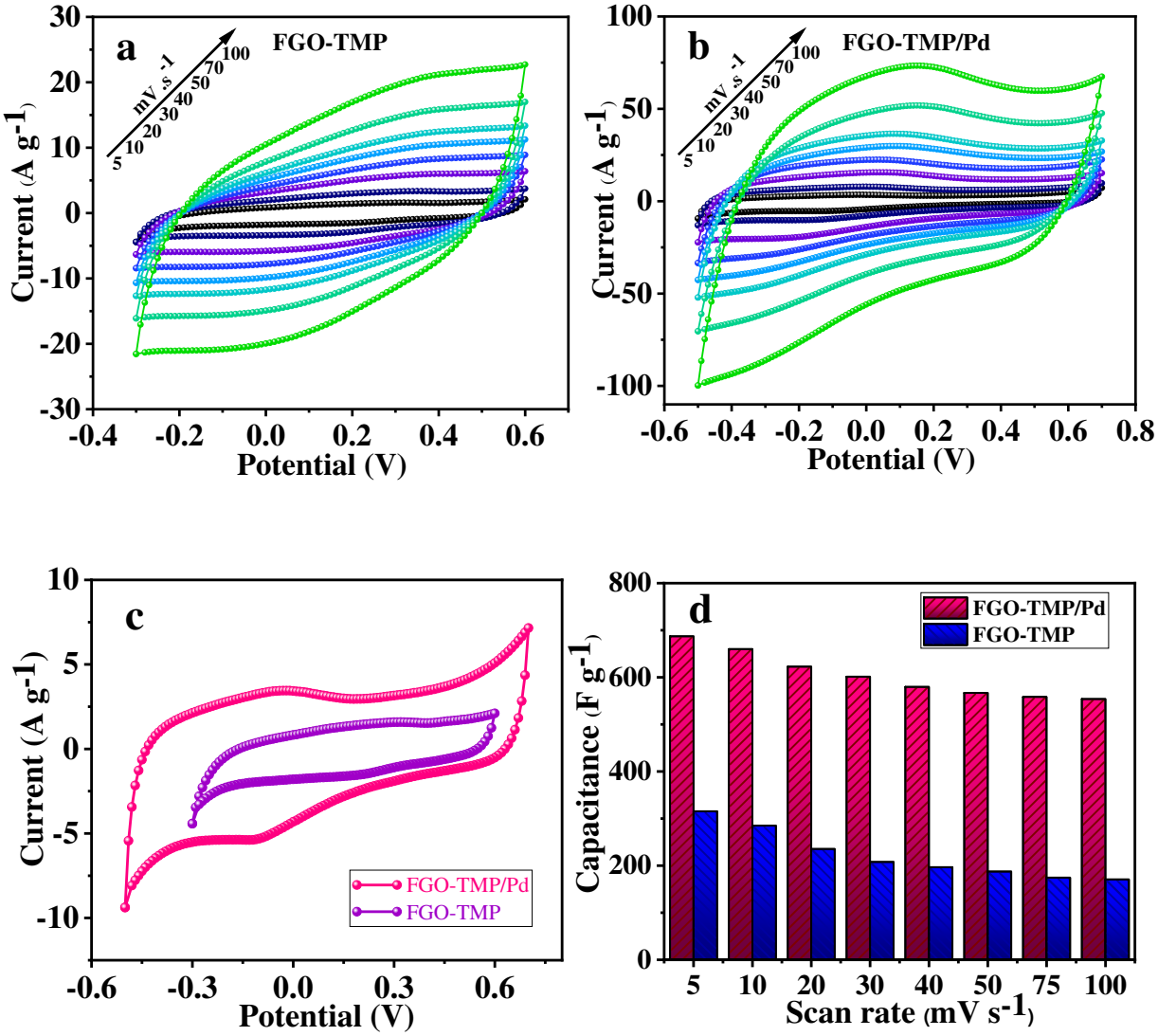

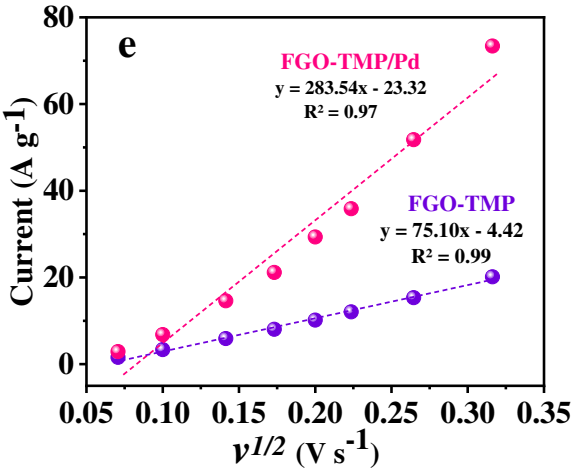


**Fig. 8.** CV scans of a) FGO-TMP and b) FGO-TMP/Pd at incremental rates from 5 to 100 mV $s^{-1}$, c) CV plot of the FGO-TMP and FGO-TMP/Pd at 5 mV $s^{-1}$, and d) Specific capacitances of FGO-TMP and FGO-TMP/Pd electrodes at different scan rate. e) Randles-Sevcik plots of the FGO-TMP and FGO-TMP/Pd.

GCD tests were utilized to investigate the modified electrodes' supercapacitive efficiency under ideal circumstances. Fig. 9a shows the GCD diagrams for the improved electrodes with FGO-TMP and FGO-TMP/Pd in the described potential window, as determined by their respective CV analyses at 1.0 A $g^{-1}$ current density. All of the graphs are linear, triangular in design, symmetric, and quite sharp, as can be seen. Furthermore, the increased columbic performance, bidirectional action, and superior capacitor outcomes of specimens could be deduced using identical charging and discharging durations. GCD graphs of FGO-TMP and FGO-TMP/Pd electrodes at current densities of 0.5 to 16 A $g^{-1}$ are shown in Fig. S7a and S7b. Despite the fact that both FGO-TMP and FGO-TMP/Pd are supercapacitive, FGO-TMP/Pd has a longer discharge time (t =774.2s) than FGO-TMP (t =247.9s) at 1 A $g^{-1}$. This emphasizes FGO-TMP/Pd higher capacity and energy storage capabilities. FGO-TMP/Pd has an estimated capacitance of 645.2 F $g^{-1}$, higher than FGO-

TMP (275.4 F $g^{-1}$) at 1 A $g^{-1}$. They are also compared to the specific capacitances of Pd composites previously discussed (See Table 1). Also, the comparison of electrochemical activity of FGO-TMP and FGO-TMP-Pd with the porous graphene composites is shown in the table S4. The FGO-TMP/Pd high capacitance performance might be explained by the synergistic effect of the GO and TMP/Pd complex. The projected specific capacitance diagram based on the discharge current density is shown in Fig. 9b. As the current density grows, the values of specific capacitance decrease due to the sluggish pace of redox reactions at a high current density. Because of the good interfacial connection between the GO and TMP/Pd complex, which facilitates facile electron transport during the electrochemical examination, the FGO-TMP/Pd hybrids exhibit a remarkable electrochemical performance. We further expect that the TMP/Pd combination in GO will improve ion transport in the electrolyte, enabling access to almost all electrode pores. The specific capacity is raised as a result of the complete insertion reaction (with long cycle durability). A counter ion from the aqueous electrolyte $H_2SO_4$ stabilizes the charge on the FGO-TMP/Pd. The following mechanism governs the electrochemical reaction of FGO-TMP/Pd (Fig. S6): TMP expels hydrogen ($H^+$) and palladium ($Pd^{+2}$) ions from the complex during the charging process and absorbs $HSO_4^-$ ions to form $Pd^0$. TMP is introduced with $H^+$ ($HNO_3$) during discharging time, and $Pd^0$ ions return to $Pd^{+2}$ ions. TMP/Pd functional groups on the surface of GO sheets not only lead to a high capacitance value (EDLC and pseudocapacitance), but also prevent GO sheets from moving[36].

Moreover, the cyclic durability of materials was investigated at 8 A $g^{-1}$ for 10000 consecutive cycles using galvanostatic procedures (Fig. 9c)[68,69]. The determined capacitance preservation based on a cycle number reveals that the FGO-TMP/Pd electrodes have outstanding cyclic durability, with only a 4.2 % reduction in electrochemical consistency during the cyclic

charge/discharge operation. The capacitance preservation of FGO-TMP, on the other hand, dropped by 7.1 %. The significant improvement in electrochemical properties of FGO-TMP/Pd could be associated with a number of aspects, such as electrode activation, that mainly increases the accessible electroactive regions in enormous quantity and enhances electrolyte functionality and the presence of TMP/Pd ligands with superior supercapacitive efficiency than FGO-TMP. Also, the SC data and cycling durability of the electrodes were appraised from GCD plots and remarkably matched the CV measurements. The inclusion of TMP/Pd in the composites, which can operate as obstacles to inhibit GO restacking, may account for the improved stability of FGO-TMP/Pd. On the surface of GO, the TMP/Pd combination can function as a conductive route for enhanced electrochemical behavior and cyclability. More Importantly, the synergistic action of TMP, Pd metal, and GO decrease the surface resistance and ion diffusion of electrode/electrolyte, providing an excellent channel for better electrochemical activity.

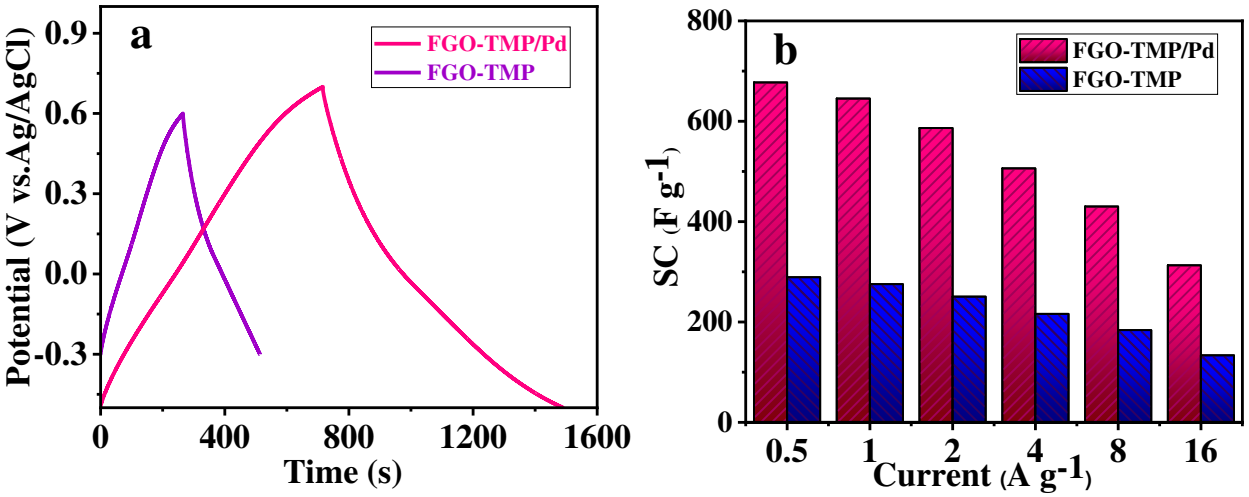

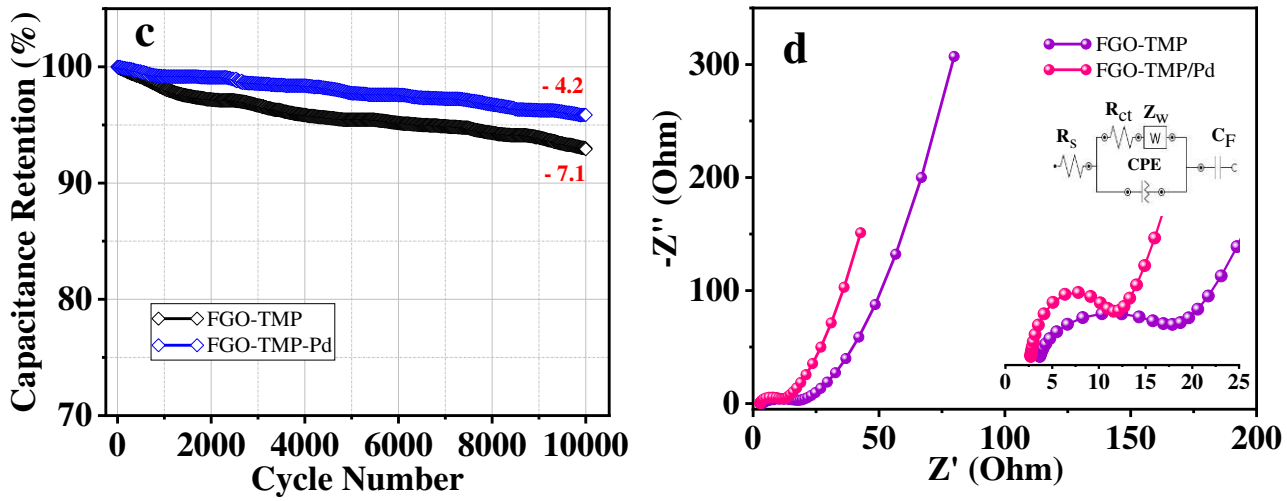


**Fig. 9.** a) Charge-discharge plots of the FGO-TMP and FGO-TMP/Pd at 1 A $g^{-1}$, b) The capacitance of the FGO-TMP and FGO-TMP/Pd at different current density values from 0.5 to 16 A $g^{-1}$, c) Cyclic stability plot of the FGO-TMP and FGO-TMP/Pd at 8 A $g^{-1}$, and d) Nyquist plot of the FGO-TMP and FGO-TMP/Pd based supercapacitor in $H_2SO_4$ electrolyte and the corresponding equivalent circuit simulation results.

**Table 1.** Different values of Method, electrolyte, specific capacitance, and cycle stability for Pd composite electrodes compared with FGO-TMP and FGO-TMP/Pd composite.

| Materials | Method | Electrolyte | Specific capacitance (F $g^{-1}$) | Cycling stability | Ref. |
|---|---|---|---|---|---|
| $Pd/MnO_x$ | Electrodeposition | 0.5 M $Na_2SO_4$ | 186 F $g^{-1}$ at (1 mA $cm^{-2}$) | 95% over 250 cycles | [70] |
| $Pd\text{-}WO_3$ | Hydrothermal method | 1 M $Na_2SO_4$ | 34 F $g^{-1}$ at (0.5 A $g^{-1}$) | 86.9% over 1100 cycles | [71] |
| Pd@CdIF-8 | Hydrothermal method | 7 M KOH | 502 F $g^{-1}$ at (0.05 A $g^{-1}$) | 83.6% over 10000 cycles | [72] |
| PdO/PPy<br>PdO/PPy/rGO | Electrodeposition method | 1 M $H_2SO_4$ | 335 F $g^{-1}$<br>595 F $g^{-1}$ at (1 A $g^{-1}$) | -<br>88% over 5000 cycles | [36] |

| | | | | | |
|---|---|---|---|---|---|
| $Pd/MoO_3$ | Hydrothermal method | 1 M $Na_2SO_4$ | 501 F $g^{-1}$ at (1 mA $g^{-1}$) | 94% over 1000 cycles | [73] |
| 3D-Pd/rGO nanostructure | Hydrothermal method | 0.5 M $H_2SO_4$ | 582.8 F $g^{-1}$ at (2 mV $s^{-1}$) | 92.7% over 3000 cycles | [74] |
| rGO/CNT@Pd + PANI Nf | Hydrothermal route | 2 M $H_2SO_4$ | 611.8 F $g^{-1}$ at (1.5 A $g^{-1}$) | 84.3% over 10000 cycles | [75] |
| Pd NPs-graphene | Chemical approach | 1M KCl | 637 F $g^{-1}$ at (1.25 A $g^{-1}$) | 91.4% over 10000 cycles | [76] |
| GO@NHC-Pd | Multistep approach | 0.5 M $K_2SO_4$ | 105.3 F $g^{-1}$ at (0.1 A $g^{-1}$) | 96.9% over 2500 cycles | [77] |
| **FGO-TMP**<br>**FGO-TMP/Pd** | **Chemical method** | **1 M $H_2SO_4$** | **315 F $g^{-1}$**<br>**687 F $g^{-1}$**<br>**at (1 A $g^{-1}$)** | **92.9%**<br>**95.8%**<br>**over 10000 cycles** | **This Work** |

The EIS method was used to explore the depth of the internal charge transfer processes at the electrode/electrolyte contact. The Nyquist plots of FGO-TMP and FGO-TMP/Pd are shown in Fig. 9d. EIS experiments were performed using a DC potential of roughly -0.45 V and a 5 mV AC potential throughout a frequency range of 10 mHz to 100 kHz. The equivalent circuit depicts a diffusion-controlled process in low-frequency regions as a linear graph. It consists of five distinct elements of $R_{ct}$ (charge transfer resistance), $R_s$ (bulk solution), CPE (constant phase element), $C_F$ (maximum pseudocapacitance), and $Z_w$ (Warburg impedance), which could be used to implement the result of EIS assessment[78,79]. The FGO-TMP/Pd electrode has a lower $R_{ct}$ (8.51) than FGO-TMP (13.72), suggesting superior electrical characteristics. The FGO-TMP/Pd electrode exhibits good electrical conductivity and an acceptable $R_{ct}$ value for practical supercapacitor applications. Reduced charge collection on the electrode surface and capacitive performance in high-frequency zones are also caused by the aforementioned charge transfer process. Nyquist plots, on the other hand, show the morphology of a vertical line as it moves toward the imaginary part Z" axis by increasing the impedance real part (Z') over low-frequency zones as a result of diffusion resistance caused by ion transport restriction[80]. The FGO-TMP/Pd electrode demonstrated remarkable

pseudocapacitive performance in low-frequency zones based on the parameters mentioned above. The FGO-TMP/Pd electrode also seems to have a greater slope, implying a lower Rs value (2.71 Ω) than the FGO-TMP electrode (3.64 Ω). The $Z_w$ is a straight line at low frequencies, and these graphs indicate the lengths of ion diffusion paths. FGO-TMP and FGO-TMP/Pd have $Z_w$ of 0.44 and 0.61, respectively. As we can see, modifying FGO-TMP resulted in shorter ion diffusion paths and fewer ion transport impediments. Finally, as demonstrated in Table 2, the FGO-TMP/Pd electrode electrochemically outperforms the FGO-TMP electrode.

**Table. 2.** Calculated EIS parameters by the CNLS fitting of experimental impedance.

| | $R_s$ (Ω) | CPE-Y0 (mF) | CPE-N | $Z_w$ | $R_{ct}$ (Ω) | $C_F$ (mF) |
|---|---|---|---|---|---|---|
| **FGO-TMP** | 3.64 | 0.31 | 0.84 | 0.44 | 13.72 | 60.12 |
| **FGO-TMP/Pd** | 2.71 | 0.45 | 0.88 | 0.61 | 8.51 | 153.63 |

## 7. Electrochemical behaviour of a symmetrically arranged supercapacitor

In an SSC cell with a 1M $H_2SO_4$ electrolyte, the electrochemical behavior of the samples was also investigated. FGO-TMP/Pd//FGO-TMP/Pd and FGO-TMP//FGO-TMP have standard CV curve forms ranging from 0 to 1.2 and 0 to 0.9 V, respectively. Fig. 10a and 10b show the symmetrical systems' CV curves at scan rates ranging from 5 to 100 mV $s^{-1}$. The prospective window had a more substantial backdrop when the sweep rate was increased. It is generally known that CV patterns with a well-defined rectangular form result in lower charge transfer resistance and, as a result, a greater ion diffusion rate. Fig. 10c is the CV of the asymmetric supercapacitor with FGO-TMP/Pd//FGO-TMP/Pd and FGO-TMP//FGO-TMP at 50 mV $s^{-1}$ in the 1 M $H_2SO_4$ solution. The approximately optimum rectangular shape was created from FGO-TMP/Pd composite modified

electrode, delivering an ideal capacitive performance owing to the presence of Pd as a conductive/electroactive structure, according to the findings of Fig. 10a. In addition, in Fig. 10d, the SC vs. sweep rate fluctuations are shown. At 5 mV $s^{-1}$, cells comprising FGO-TMP/Pd//FGO-TMP/Pd and FGO-TMP//FGO-TMP had specific capacitances of 330 and 157 F $g^{-1}$, respectively.

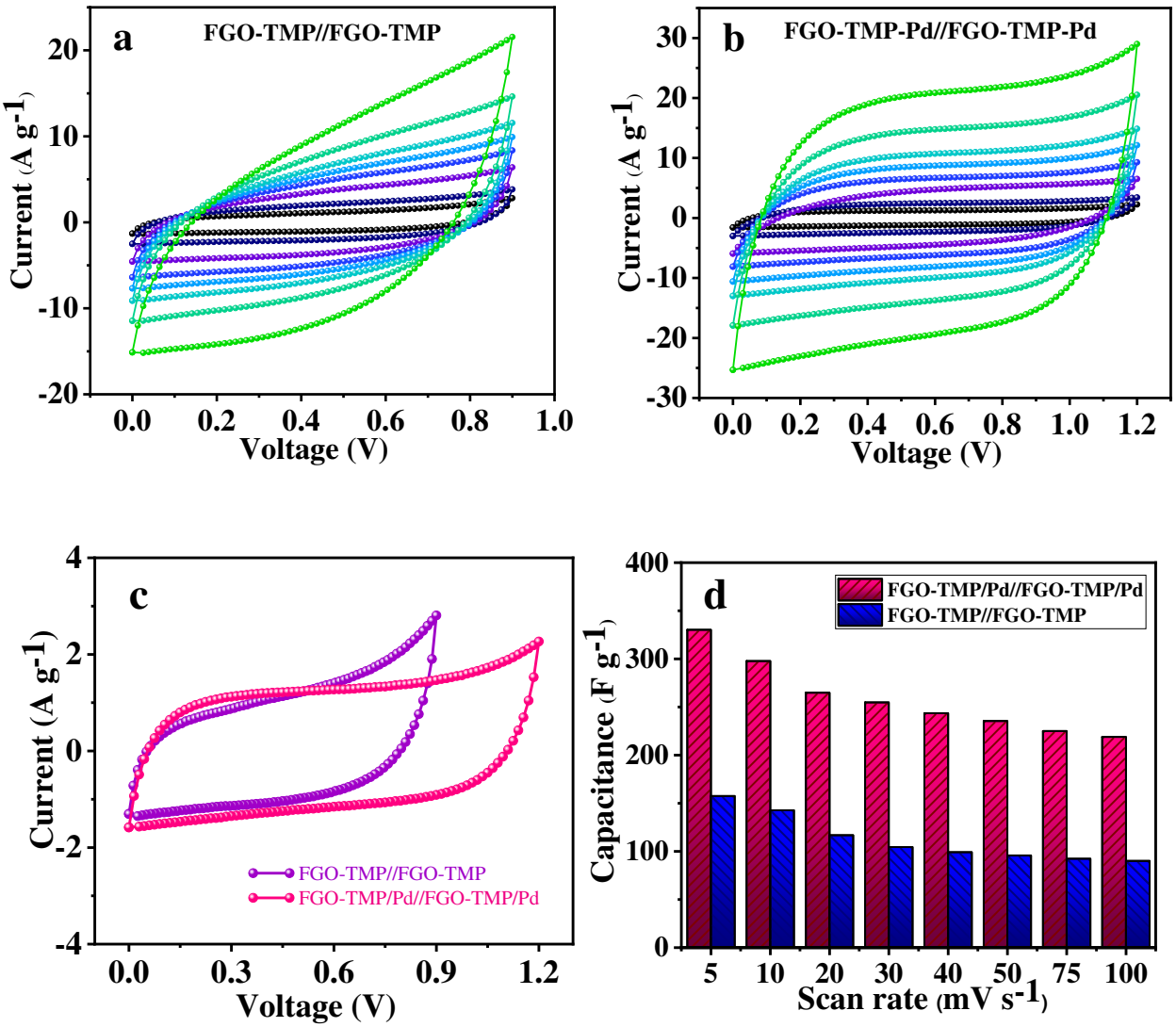


**Fig. 10.** CV scans of a) FGO-TMP//FGO-TMP and b) FGO-TMP/Pd//FGO-TMP/Pd at incremental rates from 5 to 100 mV $s^{-1}$; c) CV plot of the FGO-TMP//FGO-TMP and FGO-TMP/Pd//FGO-TMP/Pd at 5

mV $s^{-1}$, and d) Specific capacitances of FGO-TMP//FGO-TMP and FGO-TMP/Pd//FGO-TMP/Pd electrodes at different scan rate.

Fig. 11a shows charge/discharge diagrams for FGO-TMP/Pd and FGO-TMP symmetric devices at 1 A $g^{-1}$. GCD graphs for two produced electrodes at varying current densities are also shown in Fig. S7c and S7d. These figures display symmetric shapes when viewed at varying current densities, revealing their distinctive supercapacitive character. The SC graphs vs. current density are given in Fig. 11b. At 1 A $g^{-1}$, the FGO-TMP/Pd/FGO-TMP/Pd and FGO-TMP/FGO-TMP devices had specific capacitances of 287 and 139 F $g^{-1}$, respectively.

In Fig. 11c, the specific capacitance of the FGO-TMP/Pd//FGO-TMP/Pd electrode retains roughly 93.7 percent of its original value, while the FGO-TMP//FGO-TMP electrode retains 91.9 percent of its initial capacitance value after 10000 cycles. This cyclic stability test shows that FGO-TMP/Pd has high electrochemical stability in SSC devices. Furthermore, as shown in Fig. 11d, the GCD findings were used to calculate $E_d$ and $P_d$. The as-designed FGO-TMP/Pd//FGO-TMP/Pd system indicated an $E_d$ of 60.3, 57.5, 52.2, 45.9, 36.7, and 26.2 W h $kg^{-1}$ at respective $P_d$ of 1200, 2400, 4800, 9600, 19200 and 38400 W $kg^{-1}$. The FGO-TMP//FGO-TMP demonstrate $E_d$ value of 16.4, 15.6, 14.2, 12.5, 10.1, and 7.2 W h $kg^{-1}$ at 900, 1800, 3600, 7200, 14400 and 28800 W $kg^{-1}$, which outperforms several recently published devices, such as Pd-$WO_3$ (10.6 W h $kg^{-1}$ at 198 W $kg^{-1}$)[71], Pd@CdIF-8 (78.85 W h $kg^{-1}$ at 493 W $kg^{-1}$)[72], Pd/$MoO_3$ (69.58 W h $kg^{-1}$ at 249 W $kg^{-1}$)[73], rGO/CNT@Pd + PANI Nf (85 W h $kg^{-1}$ at 10200 W $kg^{-1}$)[75], and Pd NPs-graphene (56 W h $kg^{-1}$ at 1166 W $kg^{-1}$)[76].

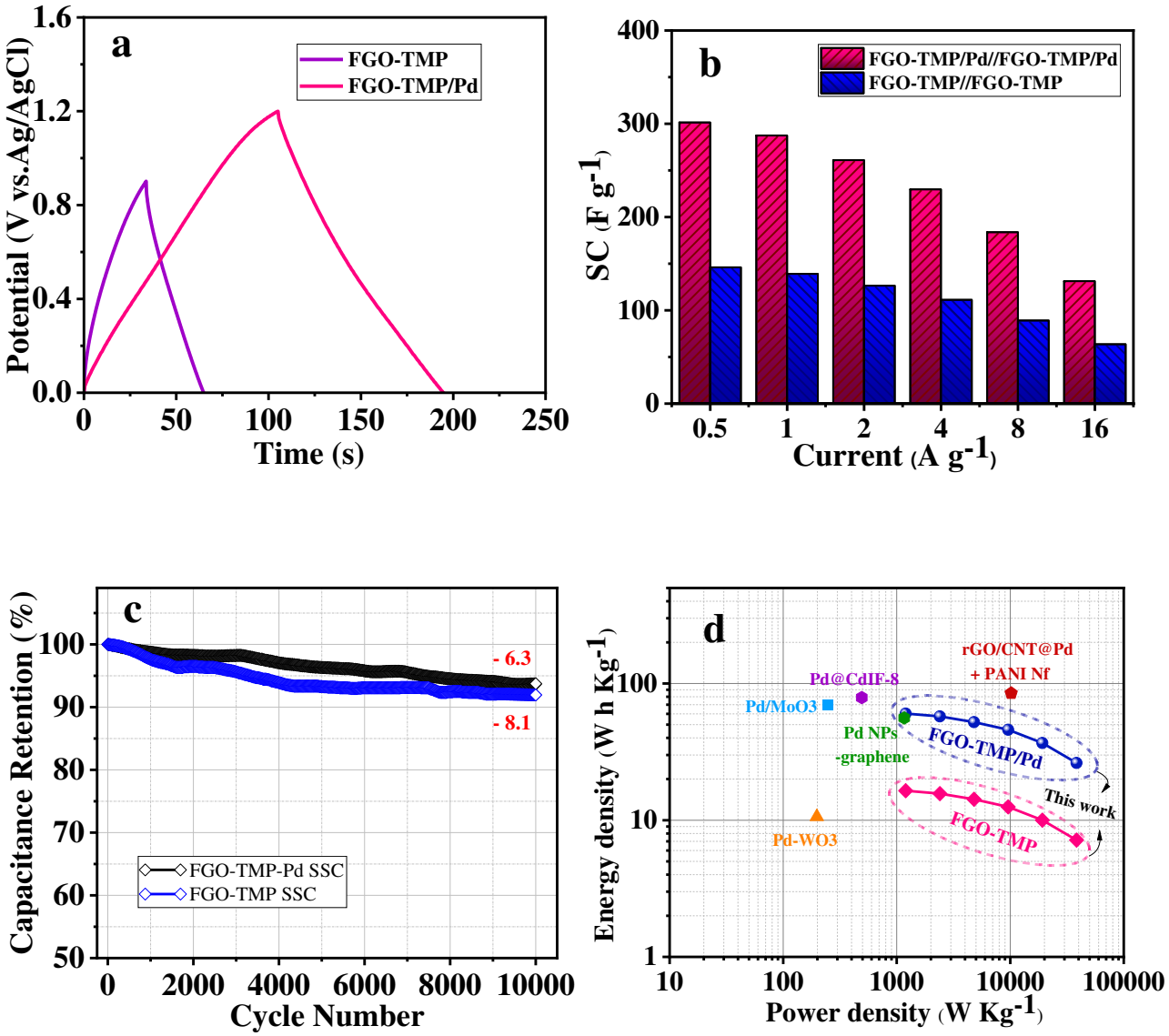


**Fig. 11.** a) charge-discharge plots of FGO-TMP//FGO-TMP and FGO-TMP/Pd//FGO-TMP/Pd at 1 A $g^{-1}$; b) The capacitance of the FGO-TMP//FGO-TMP and FGO-TMP/Pd//FGO-TMP/Pd at different current density values from 0.5 to 16 A $g^{-1}$ c) Cyclic stability plot of the FGO-TMP//FGO-TMP and FGO-TMP/Pd//FGO-TMP/Pd at 8 A $g^{-1}$; d) comparison of FGO-TMP//FGO-TMP and FGO-TMP/Pd//FGO-TMP/Pd with others[71–73,75,76] in a Ragone plot.

## 8. Conclusion

This study created and confirmed chemically synthesized FGO-TMP and FGO-TMP/Pd using DFT, various surface studies, and various electrochemical methods. Palladium ions were reacted and fixed on the surface of the FGO-TMP composite, resulting in enhanced electron transport (doping process) between the electrode/electrolyte interface and, as a result, improved supercapacitive functioning of the constructed device. Within a three-electrode cell, the manufactured composite of FGO-TMP/Pd had a capacity of 687 F $g^{-1}$ at 5 mV $s^{-1}$, which was higher than that of FGO-TMP (315 F $g^{-1}$). The increased specific capacitance of the FGO-TMP/Pd composite is due to the synergistic effect of individual elements. The charge transport capabilities of TMP/Pd are combined with the unique structure of GO on the electrode/electrolyte interface, resulting in potential palladium-based supercapacitor electrode materials. In a 1M $H_2SO_4$ electrolyte, FGO-TMP/Pd//FGO-TMP/Pd demonstrated good capacitance (330 F $g^{-1}$ at 5 mV $s^{-1}$) and capacitance retention of 93.7 percent for symmetric arrangement. The FGO-TMP/Pd//FGO-TMP/Pd device also achieved a high value of $E_d$ (60.3 W h $kg^{-1}$) at 1200 W $kg^{-1}$. According to the topological calculations performed in this work, FGO-TMP/Pd has a greater charge distribution than FGO-TMP, making it more effective as a supercapacitor electrode material. In this approach, combining palladium ions with graphene-based composites has a lot of potential for improving the electrochemical properties of future energy storage systems.

**Acknowledgment**

The authors appreciate the financial assistance obtained from the Research Affairs Division of Amirkabir University of Technology (AUT) in Tehran, Iran. Author Seeram Ramakrishna acknowledges the IAF-PP project- R-265-000-A50-281 “Sustainable Tropical Data Centre Test Bed” awarded by the National Research Foundation of Singapore. Via our membership of the UK’s HEC Materials Chemistry Consortium, which is funded by EPSRC (EP/R029431), this work

used the ARCHER2 UK National Supercomputing Service (http://archer2.ac.uk). This work has also used the computational facilities of the Advanced Research Computing at Cardiff (ARCCA) Division, Cardiff University, and HPC Wales.

## References

[1] R. Kumar, E. Joanni, R. Savu, M.S. Pereira, R.K. Singh, C.J.L. Constantino, L.T. Kubota, A. Matsuda, S.A. Moshkalev, Fabrication and electrochemical evaluation of micro-supercapacitors prepared by direct laser writing on free-standing graphite oxide paper, Energy. 179 (2019) 676–684. https://doi.org/10.1016/j.energy.2019.05.032.

[2] R. Kumar, S. Sahoo, E. Joanni, R.K. Singh, W.K. Tan, K.K. Kar, A. Matsuda, Recent progress in the synthesis of graphene and derived materials for next generation electrodes of high performance lithium ion batteries, Progress in Energy and Combustion Science. 75 (2019) 100786. https://doi.org/10.1016/j.pecs.2019.100786.

[3] Y. Zhao, X. Zhang, W. Hua, Review of preparation technologies of organic composite phase change materials in energy storage, Journal of Molecular Liquids. 336 (2021) 115923. https://doi.org/10.1016/j.molliq.2021.115923.

[4] A. Muzaffar, M.B. Ahamed, K. Deshmukh, J. Thirumalai, A review on recent advances in hybrid supercapacitors: Design, fabrication and applications, Renewable and Sustainable Energy Reviews. 101 (2019) 123–145. https://doi.org/10.1016/j.rser.2018.10.026.

[5] M. Eskandari, N. Shahbazi, A. V. Marcos, R. Malekfar, P. Taboada, Facile MOF-derived NiCo2O4/r-GO nanocomposites for electrochemical energy storage applications, Journal of Molecular Liquids. 348 (2022) 118428. https://doi.org/10.1016/j.molliq.2021.118428.

[6] M.A. Deyab, T. Stankulov, E. Slavcheva, A.E. Awadallah, S.M. ElSaeed, E.G. Zaki, Design and

synthesis of FeMoO4/CuO for electrochemical energy storage system, Journal of Molecular Liquids. 314 (2020) 113693. https://doi.org/10.1016/j.molliq.2020.113693.

[7] T. Méndez-Morales, N. Ganfoud, Z. Li, M. Haefele, B. Rotenberg, M. Salanne, Performance of microporous carbon electrodes for supercapacitors: Comparing graphene with disordered materials, Energy Storage Materials. 17 (2019) 88–92. https://doi.org/10.1016/j.ensm.2018.11.022.

[8] M. Sethi, U.S. Shenoy, D.K. Bhat, Porous graphene-NiCo2O4 nanorod hybrid composite as a high performance supercapacitor electrode material, New Journal of Chemistry. 44 (2020) 4033–4041. https://doi.org/10.1039/c9nj05725k.

[9] M. Sethi, H. Bantawal, U.S. Shenoy, D.K. Bhat, Eco-friendly synthesis of porous graphene and its utilization as high performance supercapacitor electrode material, Journal of Alloys and Compounds. 799 (2019) 256–266. https://doi.org/10.1016/j.jallcom.2019.05.302.

[10] M. Sethi, U.S. Shenoy, D.K. Bhat, A porous graphene-NiFe2O4nanocomposite with high electrochemical performance and high cycling stability for energy storage applications, Nanoscale Advances. 2 (2020) 4229–4241. https://doi.org/10.1039/d0na00440e.

[11] M. Sethi, U.S. Shenoy, D.K. Bhat, Simple solvothermal synthesis of porous graphene-NiO nanocomposites with high cyclic stability for supercapacitor application, Journal of Alloys and Compounds. 854 (2021) 157190. https://doi.org/10.1016/j.jallcom.2020.157190.

[12] H. Bantawal, M. Sethi, U.S. Shenoy, D.K. Bhat, Porous Graphene Wrapped SrTiO3 Nanocomposite: Sr-C Bond as an Effective Coadjutant for High Performance Photocatalytic Degradation of Methylene Blue, ACS Applied Nano Materials. 2 (2019) 6629–6636. https://doi.org/10.1021/acsanm.9b01513.

[13] Y. Chen, Z. Liu, L. Sun, Z. Lu, K. Zhuo, Nitrogen and sulfur co-doped porous graphene aerogel as an efficient electrode material for high performance supercapacitor in ionic liquid electrolyte,

Journal of Power Sources. 390 (2018) 215–223. https://doi.org/10.1016/j.jpowsour.2018.04.057.

[14] X. Yu, Y. Kang, H.S. Park, Sulfur and phosphorus co-doping of hierarchically porous graphene aerogels for enhancing supercapacitor performance, Carbon. 101 (2016) 49–56. https://doi.org/10.1016/j.carbon.2016.01.073.

[15] L. Wang, Y. Ouyang, X. Jiao, X. Xia, W. Lei, Q. Hao, Polyaniline-assisted growth of MnO2 ultrathin nanosheets on graphene and porous graphene for asymmetric supercapacitor with enhanced energy density, Chemical Engineering Journal. 334 (2018) 1–9. https://doi.org/10.1016/j.cej.2017.10.005.

[16] C. Ma, L. Peng, Y. Feng, J. Shen, Z. Xiao, K. Cai, Y. Yu, Y. Min, A.J. Epstein, Polyfurfuryl alcohol spheres template synthesis of 3D porous graphene for high-performance supercapacitor application, Synthetic Metals. 220 (2016) 227–235. https://doi.org/10.1016/j.synthmet.2016.06.008.

[17] S. Dai, Z. Liu, B. Zhao, J. Zeng, H. Hu, Q. Zhang, D. Chen, C. Qu, D. Dang, M. Liu, A high-performance supercapacitor electrode based on N-doped porous graphene, Journal of Power Sources. 387 (2018) 43–48. https://doi.org/10.1016/j.jpowsour.2018.03.055.

[18] S.K. Shinde, M.B. Jalak, G.S. Ghodake, N.C. Maile, V.S. Kumbhar, D.S. Lee, V.J. Fulari, D.Y. Kim, Chemically synthesized nanoflakes-like NiCo 2 S 4 electrodes for high-performance supercapacitor application, Applied Surface Science. 466 (2019) 822–829. https://doi.org/10.1016/j.apsusc.2018.10.100.

[19] S.K. Shinde, S. Ramesh, C. Bathula, G.S. Ghodake, D.Y. Kim, A.D. Jagadale, A.A. Kadam, D.P. Waghmode, T.V.M. Sreekanth, H.S. Kim, P.C. Nagajyothi, H.M. Yadav, Novel approach to synthesize NiCo2S4 composite for high-performance supercapacitor application with different molar ratio of Ni and Co, Scientific Reports. 9 (2019) 13717. https://doi.org/10.1038/s41598-019-50165-5.

[20] R.Z. Zhang, X.H. Cui, S.S. Li, X.H. Li, H.L. Cui, DFT computation of quantum capacitance of transition-metals and vacancy doped Sc2CF2 MXene for supercapacitor applications, Journal of Molecular Liquids. 345 (2022) 118263. https://doi.org/10.1016/j.molliq.2021.118263.

[21] X. Shi, S. Zheng, Z.S. Wu, X. Bao, Recent advances of graphene-based materials for high-performance and new-concept supercapacitors, Journal of Energy Chemistry. 27 (2018) 25–42. https://doi.org/10.1016/j.jechem.2017.09.034.

[22] R. Kumar, M.M. Abdel-Galeil, K.Z. Ya, K. Fujita, W.K. Tan, A. Matsuda, Facile and fast microwave-assisted formation of reduced graphene oxide-wrapped manganese cobaltite ternary hybrids as improved supercapacitor electrode material, Applied Surface Science. 481 (2019) 296–306. https://doi.org/10.1016/j.apsusc.2019.03.085.

[23] W. Yang, M. Ni, X. Ren, Y. Tian, N. Li, Y. Su, X. Zhang, Graphene in Supercapacitor Applications, Current Opinion in Colloid and Interface Science. 20 (2015) 416–428. https://doi.org/10.1016/j.cocis.2015.10.009.

[24] G.A.M. Ali, M.R. Thalji, W.C. Soh, H. Algarni, K.F. Chong, One-step electrochemical synthesis of MoS2/graphene composite for supercapacitor application, Journal of Solid State Electrochemistry. 24 (2020) 25–34. https://doi.org/10.1007/s10008-019-04449-5.

[25] Y. Xu, C. Huang, A. Hu, Z. Fan, C. Chen, Y. Yang, Q. Tang, C. Jiang, X. Chen, N-rich reduced graphene oxide film with cross-coupled porous networks as free-standing electrode for high performance supercapacitors, Applied Surface Science. 563 (2021) 150303. https://doi.org/10.1016/j.apsusc.2021.150303.

[26] R. Kumar, R. Matsuo, K. Kishida, M.M. Abdel-Galeil, Y. Suda, A. Matsuda, Homogeneous reduced graphene oxide supported NiO-MnO 2 ternary hybrids for electrode material with improved capacitive performance, Electrochimica Acta. 303 (2019) 246–256. https://doi.org/10.1016/j.electacta.2019.02.084.

[27] K.P. Annamalai, X. Zheng, J. Gao, T. Chen, Y. Tao, Nanoporous ruthenium and manganese oxide nanoparticles/reduced graphene oxide for high-energy symmetric supercapacitors, Carbon. 144 (2019) 185–192. https://doi.org/10.1016/j.carbon.2018.11.073.

[28] Z. Cao, R. Li, P. Xu, N. Li, H. Zhu, Z. Li, Highly dispersed RuO2-biomass carbon composite made by immobilization of ruthenium and dissolution of coconut meat with octyl ammonium salicylate ionic liquid for high performance flexible supercapacitor, Journal of Colloid and Interface Science. 606 (2022) 424–433. https://doi.org/10.1016/j.jcis.2021.08.011.

[29] T. Jayabalan, S. Naina Mohamed, M. Matheswaran, T.K. Radhakrishnan, A. Pugazhendhi, A. Alagarsamy, Enhanced biohydrogen production from sugar industry effluent using nickel oxide and cobalt oxide as cathode nanocatalysts in microbial electrolysis cell, International Journal of Energy Research. 45 (2021) 17431–17439. https://doi.org/10.1002/er.5645.

[30] N.I. Chandrasekaran, H. Muthukumar, A.D. Sekar, A. Pugazhendhi, M. Manickam, High-performance asymmetric supercapacitor from nanostructured tin nickel sulfide (SnNi2S4) synthesized via microwave-assisted technique, Journal of Molecular Liquids. 266 (2018) 649–657. https://doi.org/10.1016/j.molliq.2018.06.084.

[31] L. Que, L. Zhang, C. Wu, Y. Zhang, C. Pei, F. Nie, Pt-decorated graphene network materials for supercapacitors with enhanced power density, Carbon. 145 (2019) 281–289. https://doi.org/10.1016/j.carbon.2019.01.048.

[32] R. Sha, S. Badhulika, Binder free platinum nanoparticles decorated graphene-polyaniline composite film for high performance supercapacitor application, Electrochimica Acta. 251 (2017) 505–512. https://doi.org/10.1016/j.electacta.2017.08.140.

[33] E. Azizi, J. Arjomandi, J.Y. Lee, Reduced graphene Oxide/Poly(1,5 dihydroxynaphthalene)/TiO 2 nanocomposite conducting polymer coated on gold as a supercapacitor electrode, Electrochimica Acta. 298 (2019) 726–734. https://doi.org/10.1016/j.electacta.2018.12.074.

[34] V.K. Gupta, A. Fakhri, S. Agarwal, M. Naji, Palladium oxide nanoparticles supported on reduced graphene oxide and gold doped: Preparation, characterization and electrochemical study of supercapacitor electrode, Journal of Molecular Liquids. 249 (2018) 61–65. https://doi.org/10.1016/j.molliq.2017.11.016.

[35] P.K. Kalambate, C.R. Rawool, S.P. Karna, A.K. Srivastava, Nitrogen-doped graphene/palladium nanoparticles/porous polyaniline ternary composite as an efficient electrode material for high performance supercapacitor, Materials Science for Energy Technologies. 2 (2019) 246–257. https://doi.org/10.1016/j.mset.2018.12.005.

[36] J. Jose, S.P. Jose, T. Prasankumar, S. Shaji, S. Pillai, S.P. B, Emerging ternary nanocomposite of rGO draped palladium oxide/polypyrrole for high performance supercapacitors, Journal of Alloys and Compounds. 855 (2021) 157481. https://doi.org/10.1016/j.jallcom.2020.157481.

[37] I.S. El-Hallag, M.N. El-Nahass, S.M. Youssry, R. Kumar, M.M. Abdel-Galeil, A. Matsuda, Facile in-situ simultaneous electrochemical reduction and deposition of reduced graphene oxide embedded palladium nanoparticles as high performance electrode materials for supercapacitor with excellent rate capability, Electrochimica Acta. 314 (2019) 124–134. https://doi.org/10.1016/j.electacta.2019.05.065.

[38] V. Sridhar, H.J. Kim, J.H. Jung, C. Lee, S. Park, I.K. Oh, Defect-engineered three-dimensional graphene-nanotube-palladium nanostructures with ultrahigh capacitance, ACS Nano. 6 (2012) 10562–10570. https://doi.org/10.1021/nn3046133.

[39] E. Kowsari, F. Morad, N. Seifvand, B. Bazri, M. Karimi, Synthesis of reduced graphene oxide functionalized with methyl red dye and its role in enhancing photoactivity in TiO2–IL/WO3 composite for toluene degradation, Research on Chemical Intermediates. 46 (2020) 1217–1234. https://doi.org/10.1007/s11164-019-04030-9.

[40] C.M. Maroneze, A. Rahim, N. Fattori, L.P. Da Costa, F.A. Sigoli, I.O. Mazali, R. Custodio, Y.

Gushikem, Electroactive Properties of 1-propyl-3-methylimidazolium Ionic Liquid Covalently Bonded on Mesoporous Silica Surface: Development of an Electrochemical Sensor Probed for NADH, Dopamine and Uric Acid Detection, Electrochimica Acta. 123 (2014) 435–440. https://doi.org/10.1016/j.electacta.2014.01.071.

[41] N. Seifvand, E. Kowsari, Novel TiO2/graphene oxide functionalized with a cobalt complex for significant degradation of NOx and CO, RSC Advances. 5 (2015) 93706–93716. https://doi.org/10.1039/c5ra13620b.

[42] S.E.M. Pourhosseini, O. Norouzi, P. Salimi, H.R. Naderi, Synthesis of a Novel Interconnected 3D Pore Network Algal Biochar Constituting Iron Nanoparticles Derived from a Harmful Marine Biomass as High-Performance Asymmetric Supercapacitor Electrodes, ACS Sustainable Chemistry and Engineering. 6 (2018) 4746–4758. https://doi.org/10.1021/acssuschemeng.7b03871.

[43] S. Alireza Hashemi, S. Mojtaba Mousavi, H. Reza Naderi, S. Bahrani, M. Arjmand, A. Hagfeldt, W.H. Chiang, S. Ramakrishna, Reinforced polypyrrole with 2D graphene flakes decorated with interconnected nickel-tungsten metal oxide complex toward superiorly stable supercapacitor, Chemical Engineering Journal. 418 (2021) 129396. https://doi.org/10.1016/j.cej.2021.129396.

[44] S.K. Shinde, H.M. Yadav, S. Ramesh, C. Bathula, N. Maile, G.S. Ghodake, H. Dhaygude, D.-Y. Kim, High-performance symmetric supercapacitor; nanoflower-like NiCo2O4//NiCo2O4 thin films synthesized by simple and highly stable chemical method, Journal of Molecular Liquids. 299 (2020) 112119. https://doi.org/10.1016/j.molliq.2019.112119.

[45] E. Kowsari, A. Ehsani, M. Dashti Najafi, M. Bigdeloo, Enhancement of pseudocapacitance performance of p-type conductive polymer in the presence of newly synthesized graphene oxide-hexamethylene tributylammonium iodide nanosheets, Journal of Colloid and Interface Science. 512 (2018) 346–352. https://doi.org/10.1016/j.jcis.2017.10.076.

[46] G.A.M. Ali, E. Megiel, P. Cieciórski, M.R. Thalji, J. Romański, H. Algarni, K.F. Chong, Ferrocene functionalized multi-walled carbon nanotubes as supercapacitor electrodes, Journal of Molecular Liquids. 318 (2020) 114064. https://doi.org/10.1016/j.molliq.2020.114064.

[47] N. Neekzad, E. Kowsari, M.D. Najafi, H. Reza Naderi, A. Chinnappan, S. Ramakrishna, V. Haddadi-Asl, Pseudocapacitive performance of surface functionalized halloysite nanotubes decorated green additive ionic liquid modified with ATP and POAP for efficient symmetric supercapacitors, Journal of Molecular Liquids. 342 (2021) 116962. https://doi.org/10.1016/j.molliq.2021.116962.

[48] S. Pilathottathil, T. Kannan Kottummal, M.S. Thayyil, P. Mahadevan Perumal, J. Ambichi Purakakath, Inorganic salt grafted ionic liquid gel electrolytes for efficient solid state supercapacitors: Electrochemical and dielectric studies, Journal of Molecular Liquids. 264 (2018) 72–79. https://doi.org/10.1016/j.molliq.2018.05.014.

[49] A. Rezanezhad, E. Rezaie, L.S. Ghadimi, A. Hajalilou, E. Abouzari-Lotf, N. Arsalani, Outstanding supercapacitor performance of Nd–Mn co-doped perovskite LaFeO3@nitrogen-doped graphene oxide nanocomposites, Electrochimica Acta. 335 (2020) 135699. https://doi.org/10.1016/j.electacta.2020.135699.

[50] R. Bader, Atoms in Molecules — a Quantum Theory, Journal of Molecular Structure: THEOCHEM. 360 (1994). https://books.google.es/books?id=tyVpQgAACAAJ.

[51] W. Kohn, L.J. Sham, Self-consistent equations including exchange and correlation effects, Physical Review. 140 (1965) A1133. https://doi.org/10.1103/PhysRev.140.A1133.

[52] R. Nityananda, P. Hohenberg, W. Kohn, Inhomogeneous electron gas, Resonance. 22 (2017) 809–811. https://doi.org/10.1007/s12045-017-0529-3.

[53] A.D. Becke, A new mixing of Hartree-Fock and local density-functional theories, The Journal of

Chemical Physics. 98 (1993) 1372–1377. https://doi.org/10.1063/1.464304.

[54] G. Kresse, J. Furthmüller, Efficiency of ab-initio total energy calculations for metals and semiconductors using a plane-wave basis set, Computational Materials Science. 6 (1996) 15–50. https://doi.org/10.1016/0927-0256(96)00008-0.

[55] G. Kresse, J. Furthmüller, Efficient iterative schemes for ab initio total-energy calculations using a plane-wave basis set, Physical Review B - Condensed Matter and Materials Physics. 54 (1996) 11169–11186. https://doi.org/10.1103/PhysRevB.54.11169.

[56] S. Grimme, S. Ehrlich, L. Goerigk, Effect of the damping function in dispersion corrected density functional theory, Journal of Computational Chemistry. 32 (2011) 1456–1465. https://doi.org/10.1002/jcc.21759.

[57] D. Vega, D. Almeida, AIM-UC: An application for QTAIM analysis, Journal of Computational Methods in Sciences and Engineering. 14 (2014) 131–136. https://doi.org/10.3233/JCM-140491.

[58] M. Mohamadi, E. Kowsari, V. haddadi-Asl, M. Yousefzadeh, A. Chinnappan, S. Ramakrishna, Highly-efficient microwave absorptivity in reduced graphene oxide modified with PTA@ imidazolium based dicationic ionic liquid and fluorine atom, Composites Science and Technology. 188 (2020) 107960. https://doi.org/10.1016/j.compscitech.2019.107960.

[59] B. Peng, Y. Xu, K. Liu, X. Wang, F.M. Mulder, High-Performance and Low-Cost Sodium-Ion Anode Based on a Facile Black Phosphorus−Carbon Nanocomposite, ChemElectroChem. 4 (2017) 2140–2144. https://doi.org/10.1002/celc.201700345.

[60] B.D. Ossonon, D. Bélanger, Synthesis and characterization of sulfophenyl-functionalized reduced graphene oxide sheets, RSC Advances. 7 (2017) 27224–27234. https://doi.org/10.1039/c6ra28311j.

[61] M.D. Najafi, E. Kowsari, H.R. Naderi, A. Chinnappan, S. Ramakrishna, A. Ehsani, A. Shokravi,

Functionalization of graphene oxide via chromium complexes coordinated on 5-aminopyridine-2-carboxylic acid as a symmetric supercapacitor electrode materials in energy storage devices, Composites Science and Technology. 211 (2021) 108844. https://doi.org/10.1016/j.compscitech.2021.108844.

[62] J.R. Durig, R. Layton, D.W. Sink, B.R. Mitchell, Far infrared spectra of palladium compounds-I. The influence of ligands upon the palladium chloride stretching frequency, Spectrochimica Acta. 21 (1965) 1367–1378. https://doi.org/10.1016/0371-1951(65)80046-7.

[63] M.M. Heravi, S. Asadi, S.M. Hoseini Chopani, E. Jaderi, N-Heterocyclic Carbene–Palladium Complex onto Graphene Oxide and Poly (ethylene glycol) (PEG) Applied as Superior Catalyst for the Suzuki-Miyaura Cross-Coupling Reaction in Water, Applied Organometallic Chemistry. 34 (2020) e5805. https://doi.org/10.1002/aoc.5805.

[64] M.R. Chirani, E. Kowsari, H. SalarAmoli, M. Yousefzadeh, A. Chinnappan, S. Ramakrishna, Covalently functionalized graphene oxide with cobalt–nitrogen-enriched complex containing iodide ligand as charge carrier nanofiller for eco-friendly high performance ionic liquid-based dye-sensitized solar cell, Journal of Molecular Liquids. 325 (2021) 115198. https://doi.org/10.1016/j.molliq.2020.115198.

[65] J. Bin Wu, M.L. Lin, X. Cong, H.N. Liu, P.H. Tan, Raman spectroscopy of graphene-based materials and its applications in related devices, Chemical Society Reviews. 47 (2018) 1822–1873. https://doi.org/10.1039/c6cs00915h.

[66] A.A. Ashtiani, E. Kowsari, V. Haddadi-Asl, M. Yousefi, H.R. Naderi, A. Chinnappan, S. Ramakrishna, Pseudocapacitive efficiency of covalently Cr-complex with L-histidine-methyl ester as a ligand graphene oxide blended with conducting polymer (POAP) as electrode material in supercapacitor, Journal of Molecular Liquids. 315 (2020) 113697. https://doi.org/10.1016/j.molliq.2020.113697.

[67] T. Van Nguyen, L.T. Son, V. Van Thuy, V.D. Thao, M. Hatsukano, K. Higashimine, S. Maenosono, S.E. Chun, T.V. Thu, Facile synthesis of Mn-doped NiCo2O4 nanoparticles with enhanced electrochemical performance for a battery-type supercapacitor electrode, Dalton Transactions. 49 (2020) 6718–6729. https://doi.org/10.1039/d0dt01177k.

[68] A. Ehsani, E. Kowsari, M. Dashti Najafi, R. Safari, H. Mohammad Shiri, Influence of ionic liquid on pseudocapacitance performance of electrochemically synthesized conductive polymer: Electrochemical and theoretical investigation, Journal of Colloid and Interface Science. 500 (2017) 315–320. https://doi.org/10.1016/j.jcis.2017.04.014.

[69] S.K. Shinde, D.Y. Kim, V.G. Parale, H.H. Park, H.M. Yadav, Electrochemically synthesized nanoflowers to nanosphere-like nicuse2 thin films for efficient supercapacitor application, Metals. 10 (2020) 1–8. https://doi.org/10.3390/met10121698.

[70] T.A. Babkova, H. Fei, N.E. Kazantseva, I.Y. Sapurina, P. Saha, Enhancing the supercapacitor performance of flexible MnOxCarbon cloth electrodes by Pd-decoration, Electrochimica Acta. 272 (2018) 1–10. https://doi.org/10.1016/j.electacta.2018.03.143.

[71] S.P. Gupta, V.B. Patil, N.L. Tarwal, S.D. Bhame, S.W. Gosavi, I.S. Mulla, D.J. Late, S.S. Suryavanshi, P.S. Walke, Enhanced energy density and stability of self-assembled cauliflower of Pd doped monoclinic WO3 nanostructure supercapacitor, Materials Chemistry and Physics. 225 (2019) 192–199. https://doi.org/10.1016/j.matchemphys.2018.12.077.

[72] Y. Li, L. Xu, M.Y. Jia, L. Cui, X. Liu, X.J. Jin, Fabrication of Pd Nanocubes@CdIF-8 catalysts for highly efficient electrocatalytic sensing of H2O2 and high-performance supercapacitor, Materials and Design. 186 (2020) 108267. https://doi.org/10.1016/j.matdes.2019.108267.

[73] N. Guru Prakash, M. Dhananjaya, A. Lakshmi Narayana, O.M. Hussain, One-dimensional MoO3/Pd nanocomposite electrodes for high performance supercapacitors, Materials Research Express. 6 (2019) 85543. https://doi.org/10.1088/2053-1591/ab273e.

[74] A.A. Ensafi, E. Heydari-Soureshjani, B. Rezaei, Three-dimensional graphene promoted by palladium nanoparticles, an efficient electrocatalyst for energy production and storage, International Journal of Hydrogen Energy. 43 (2018) 9652–9662. https://doi.org/10.1016/j.ijhydene.2018.04.010.

[75] J.P. Mensing, T. Lomas, A. Tuantranont, Ammonia strengthened graphene/CNT-wrapped polyaniline-nanofiber composites loaded with palladium nanoparticles for coin cell supercapacitors, Electrochimica Acta. 263 (2018) 17–25. https://doi.org/10.1016/j.electacta.2017.12.193.

[76] R.A. Dar, L. Giri, S.P. Karna, A.K. Srivastava, Performance of palladium nanoparticle-graphene composite as an efficient electrode material for electrochemical double layer capacitors, Electrochimica Acta. 196 (2016) 547–557. https://doi.org/10.1016/j.electacta.2016.02.197.

[77] V. Kandathil, A. Siddiqa, A. Patra, B. Kulkarni, M. Kempasiddaiah, B.S. Sasidhar, S.A. Patil, C.S. Rout, S.A. Patil, NHC-Pd complex heterogenized on graphene oxide for cross-coupling reactions and supercapacitor applications, Applied Organometallic Chemistry. 34 (2020) e5924. https://doi.org/10.1002/aoc.5924.

[78] F. Boorboor Ajdari, M. Dashti Najafi, M. Izadpanah Ostad, H. reza Naderi, M. Niknam Shahrak, E. Kowsari, S. Ramakrishna, A symmetric ZnO-ZIF8//Mo-ZIF8 supercapacitor and comparing with electrochemical of Pt, Au, and Cu decorated ZIF-8 electrodes, Journal of Molecular Liquids. 333 (2021) 116007. https://doi.org/10.1016/j.molliq.2021.116007.

[79] G.A.M. Ali, E. Megiel, J. Romański, H. Algarni, K.F. Chong, A wide potential window symmetric supercapacitor by TEMPO functionalized MWCNTs, Journal of Molecular Liquids. 271 (2018) 31–39. https://doi.org/10.1016/j.molliq.2018.08.123.

[80] M. Dashti Najafi, S. Kholghi Eshkalak, B. Amiri, H.R. Naderi, E. Kowsari, A. Chinnappan, S. Ramakrishna, Green synthesis of fish skeleton-like BaSO4 nanostructures by the ionic liquid

designer template as nanofillers for supercapacitors application, Materials Today Chemistry. 23 (2022) 100633. https://doi.org/10.1016/j.mtchem.2021.100633.